The Raymond and
Beverly Sackler Faculty
of Exact Sciences
Tel Aviv University

THE SCHOOL OF PHYSICS & ASTRONOMY

Search for a heavy neutral lepton that mixes predominantly with the tau neutrino

Thesis submitted in partial fulfillment of the requirements for the M.Sc. degree in the School of Physics & Astronomy, Tel Aviv University

By

Ori Israel Fogel

The research work for the thesis has been carried out
under the supervision of

Prof. Abner Soffer

Abstract

Heavy neutral leptons (HNLs) are highly motivated as a solution to the problems of neutrino masses, dark matter and the baryon asymmetry of the universe. In light of tight limits set by previous searches for HNLs that mix with electron and muon neutrinos, we search for an HNL that mixes predominantly with the tau neutrino. Such an HNL can be produced in tau decays, which are best studied in B-factory experiments. We search for the HNL in a sample of $8.8 \cdot 10^8$ $e^+e^- \to \tau^+\tau^-$ events collected by the Belle experiment at center-of-mass energies around 10.58 GeV. The search focuses on long-lived HNLs with mass in the range 0.3-1.6 GeV exploiting the displaced-vertex signature for suppressing background. We set a new expected limit on the mixing between the HNL and ν_τ.

CONTENTS

1. INTRODUCTION

The Standard Model (SM) of particle physics, which was developed during the 20th century, represents the elementary particles in nature, and the fundamental interactions they experience with one another. The SM explains successfully diverse phenomena in physics, and all its major predictions were measured in experiments (one of their highlights was the discovery of Higgs boson in 2012). However, there are significant issues in today's physics, that cannot be explained by SM alone, and "new physics" should be formulate in order to do so.

One phenomenon that the SM is not able explain is the neutrino flavor oscillations which were observed firstly at the end of the last century. These oscillations necessitate neutrinos have mass states as well as their flavor states, while in SM the neutrinos are massless. A possible mechanism that incorporates these mass states to the SM can be derived from adding right handed neutrinos SM, in contrast to the known left handed in the SM (left and right handed refers to the neutrino's chirality). Sec. 2 elaborates about the nature neutrino oscillations and explain their relation to to right handed neutrinos. This Section also introduces the heavy neutrino lepton (HNL or N), a superposition of the left and right handed neutrinos and a new mass states, and its detection is the main challenge this thesis faces. Quite amazingly, the existence of HNLs can solve more problem in physics than just the neutrino mass origins. It can explain the baryon asymmetry of the universe via leptogenesis [1–3]. It can also provide a dark matter candidate, because the HNL's lifetime is dictated by the its mass and the mixing parameters of the particles it can decay to. If one the HNLs has sufficiently low mass and small mixing parameters, its lifetime is greater than the age of universe. [4–8].

The efforts to discover new physics take place in various frontiers, and a main one is the experiments that involve particle accelerators and detectors. Colliding particles in GeV-TeV energy scales, allow us create and observe particles which are not present in our everyday nature. This thesis focuses on Belle experiment, a particle detector which ran and collected data in the years 1999-2010. It was located at the High Energy Accelerator Research Organisation (KEK) in Tsukuba, Ibaraki Prefecture, Japan. The data was collected from the collisions produced in the KEKB particle accelerator. It should be mentioned that in the last years they superseded by their upgrades, Belle II and SuperKEKB respectively. Sec. 3 deals more deeply with the technical details of the experiment. Additionally, in Sec. 3 we will see that this experiment is a fantastic environment for studying tau lepton physics.

In light of that, this research takes advantage of the relatively large number of $\tau^+\tau^-$ events at belle, in order to search for an HNL that predominantly mixes with ν_τ in τ decays. This type of mixing is highly motivated because various collider (and non-collider) experiments have already set tight bounds on mixing parameters of the HNL and ν_e or ν_μ [9–19]. Until recently, the only published search that was directly sensitive to the $N-\nu_\tau$ mixing parameter $V_{\tau N}$ in our mass range is the one by DELPHI experiment (in the HNL mass range this thesis focuses on) [13]. Recently, BABAR also put out a search based on an invisible HNL which mixes with ν_τ. It found no signal, but set a bound on the mixing parameter in the range of 100-1300 MeV [20].

This thesis explains this new method, and describes every steps of this execution, starting from the generating of the Monte-Carlo simulation samples, and ending with the final plot

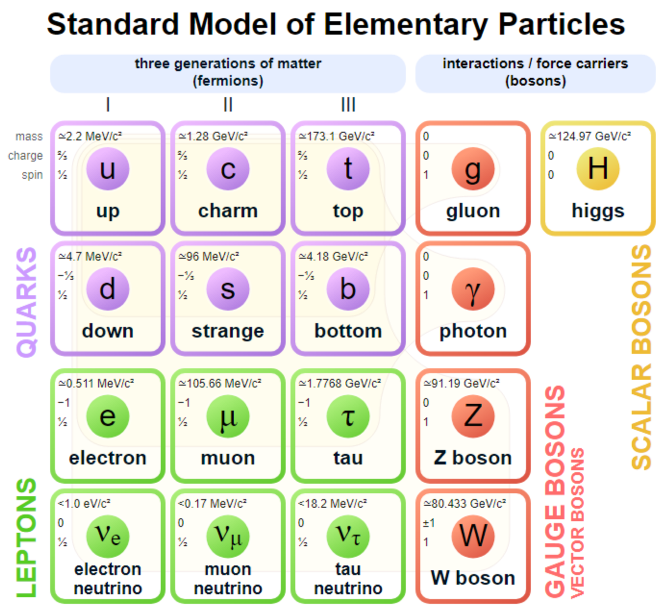

FIG. 1: The elementary particles of the Standard Model. The model contains 12 spin 1/2 fermions: 6 quarks and 6 leptons, divided into 3 flavor families (columns). 4 gauge bosons account for strong (gluon), electromagnetic (photon) and weak (Z, W) interactions. Finally, the Higgs scalar boson generates the masses of leptons and gauge bosons through the spontaneous symmetry breaking.

that presents the bound we managed to achieve on the $N - \nu_\tau$ mixing.

2. THEORETICAL OVERVIEW

2.1. The standard model

The Standard Model (SM) of particle physics describes the elementary particles and the fundamental interactions between them. Mathematically the Standard Model is a gauge theory of the strong (SU(3)) and electroweak (SU(2) x U(1)) interactions. However, gravitation is not included within the Standard Model. The elementary particles of the SM can be categorised into fermions (leptons, quarks, and their anti-particles) and to bosons. Among the elementary particles, the fermions are basically are the elementary units of matter (or anti matter), and the bosons are the force carries, responsible for the interactions between the particles. Fig. 1 presents all these particles with their chrage, mass and spin values [21].

Among the leptons, there are 3 flavors (e,μ,τ) and their corresponding neutrinos (ν_e,ν_μ,ν_τ). The neutrinos have only left-handed (LH) states, which are charged only under $\mathrm{SU(2)_L}$. However, the observations of neutrino flavor oscillations [22] indicates (according to most models) the existence of right-handed (RH) neutrino states that carry no SM gauge charges. Sections 2 2.2 and 2 2.3 explains why, and what exactly is the nature of the RH neutrino.

2.2. Neutrino flavor oscillations

As a starting point of this discussion, we assume the neutrinos have masses, and therefore, there is a spectrum of neutrino eigenstates ν_i, that their eigenvalues are these masses, which we denote by m_i. It should be mentioned that the ν_i states are different from the flavor states, which are denote here as ν_α. In fact, the two groups of states are two different bases to describe the neutrino quantum states. Therefore, we can write a flavor state in term of the mass basis (and vice versa of course) [23]:

$$|\nu_\alpha\rangle = \sum_i U_{i\alpha} |\nu_i\rangle \, , |\nu_i\rangle = \sum_i U^\dagger_{i\alpha} |\nu_\alpha\rangle \, , \tag{1}$$

Where U is called the leptonic mixing matrix, and has a completely analogous role as the CKM matrix, which is used for quark mixing in the SM. Obviously, U is unitary matrix, and the corresponding mixing matrix that takes us back from the flavor basis to the mass basis is $U^\dagger$.

In order to understand how neutrino oscillations indicate the existence of neutrinos mass states, we discuss the nature of neutrino oscillations in vacuum. Of course, we are interested of the probability of such process $P(\nu_\alpha \to \nu_\beta)$, because eventually it needs to be verified by an experiment. For that, the amplitude is needed. By using the superposition property, the amplitude can be divided into 3 contributions. If we look at a specific mass state ν_i, we need to consider the mixing matrix elements that connect this state to the initial and final states, $U^*_{\alpha i}$ and $U_{\beta i}$. The last contribution is the amplitude of ν_i propagation the distance L, which we denote as Prop(ν_i). In conclusion, we need to consider all possible ν_i states, so the final amplitude for such process is:

$$Amp(\nu_\alpha \to \nu_\beta) = \sum U_{\alpha i} Prop(\nu_i) U_{\beta i} \tag{2}$$

In order to find Prop(ν_i), Schrödinger equation needs to be solved for a neutrino with an energy E (considering that due to lightness of neutrinos, we have $E \gg m_i$). So by substituting the solution $Prop(\nu_i) = e^{-im_i^2 L/2E}$ in Eq. 2, the squared absolute value of the amplitude can be taken for getting the wanted probability:

$$\begin{aligned} P(\nu_\alpha \to \nu_\beta) = \delta_{\alpha\beta} - 4 \sum_{i>j} Re\{U_{\alpha i} U_{\beta i} U_{\alpha j} U_{\beta j}\} sin^2 \left(\frac{\Delta m^2_{ij} L}{4E} \right) \\ +2 \sum_{i>j} Im\{U_{\alpha i} U_{\beta i} U_{\alpha j} U_{\beta j}\} sin \left(\frac{\Delta m^2_{ij} L}{2E} \right) \end{aligned} \tag{3}$$

If neutrinos are massless, then $\Delta m^2_{ij} = 0$ and $P(\nu_\alpha \to \nu_\beta) = \delta_{\alpha\beta}$. It means that neutrino oscillations, namely a change in the neutrino's flavor across the distance L, indicate that the neutrinos are massive. An important note is that this phenomenon has been observed as part of experiments in which the neutrinos were passing through matter, and not only through vacuum. In some cases the neutrinos-matter interactions are negligible, but sometimes they are needed to be considered, and Eq. 3 has to be modified. Additional important fact which rises from Eq. 3, is that neutrino oscillation experiment can only tell about the neutrino squared mass splittings (the squared mass spectral pattern), as the masses' absolute differences from zero remains unknown. However, there is a limit to this difference, as the effective squared mass of the electron based neutrino mass, which is defined as $m_{\nu_e}^{2(eff)} \equiv \sum_i U_{ei}^2 m_{\nu_i}^2$, has an upper bound of 0.9 eV^2 (other flavors effective masses are relative to this) [22].

The neutrino oscillation experiments can be categorized according to the neutrino sources they deal with. In the first category there are the experiments which research solar neutrinos. Solar neutrinos, as their name implies, originate directly from nuclear activity in the sun. The main contribution comes from a proton-proton decay chain, namely: $p+p \rightarrow d+e^+ + \nu_e$. There are also other decay chains, such as ${}^8B \rightarrow {}^8Be^* + e^+ + \nu_e$, which is the one that NSO (Sudbury Neutrino Observatory) [24] used for solar neutrino detecting. The second category is atmospheric neutrinos, which are generated through interaction of incoming cosmic rays with air nuclei in Earth's atmosphere. [25] The production of these atmospheric neutrinos is dominated by the decay of $\pi \rightarrow \mu + \nu_\mu$ which is followed by $\mu \rightarrow e + \nu_\mu + \nu_e$. There are also experiments that research neutrinos from artificial sources such as nuclear reactors and particle accelerators. In conclusion, the experiments that were studying and validating the neutrino oscillation are numerous and diverse.

Eventually, the first solid discoveries of the neutrino oscillations took place in the Super-Kamiokande (atmospheric neutrinos experiment) and in NSO. The conductors of these studies were awarded the 2015 Nobel Prize for Physics for their achievements.

2.3. Right handed neutrinos

2.3.1. Neutrino mass terms

After understanding why neutrino flavor oscillations indicate the neutrinos have mass, it is now appropriate that we introduce the physical mechanism that lays the foundations for the generation of these masses [21].

For simplicity, let us add a single right handed (RH) neutrino to the SM, which we mark as ν_R (later, we can consider a more complicated model with n flavors of RH neutrinos). RH neutrinos are *sterile*, namely they do not interact via any of the SM interactions (strong, weak, electromagnetic). In other words, they are singlets of the complete SM gauge group. Moreover, the RH neutrinos couple to left handed (LH) leptons in the same way RH charged leptons couple to LH charged leptons in the SM, i.e. via Yukawa interactions. Hence, The most general renormalizable Lagrangian that is possible to write is:

$$\mathcal{L} = \mathcal{L}_{SM} + i\bar{\nu}_R \partial\!\!\!/ \nu_R - \bar{l}_L Y^\nu \nu_R \tilde{\Phi} - \frac{1}{2}\bar{\nu}_R^c M_M \nu_R + h.c. \tag{4}$$

Where $\mathcal{L}$ is the Lagrangian of the SM; the second term is the kinetic energy of the neutrino; Y^ν and M_M are the matrices of Yukawa coupling and the Majorana mass term, correspondingly (the RH neutrinos can have mass terms because such a term converts a particle to its anti-particle, which is allowed only for particles that have no conserved charge); $l_L = (\nu_L, e_L)^T$ are the left handed lepton doublets; Φ is Higgs doublet and $\tilde{\Phi} = (\epsilon\Phi)^\dagger$, where ϵ is the $SU(2)$ anti-symmetric tensor; h.c. is the hermitian conjugate of the corresponding

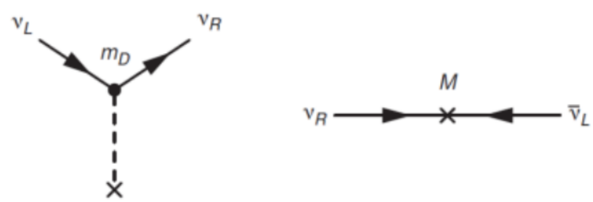

FIG. 2: Feynmann diagarams of the Dirac and Majorana mass terms, derived from Eqs. 6 and 7

terms. Additionally, the CP conjugate of ν is defined as:

$$\nu^c = CP\nu = i\gamma^2\gamma^0\nu^* \tag{5}$$

Where γ^i are the Dirac matrices.

This new Lagrangian implies on two mass terms for the RH handed neutrino. The first one is the Majorana term, which was mentioned earlier and appear explicitly in Eq. 4. The Majorana mass term involves a neutrino turning into an anti-neutrino. We can write it here:

$$\mathcal{L}_M = -\frac{1}{2}M(\bar{\nu}_R^c\nu_R + \bar{\nu}_R\nu_R^c), \tag{6}$$

The second term is the Dirac mass term. It is generated from a spontaneous electroweak symmetry breaking from the Yukawa interactions.

$$\mathcal{L}_D = -m_D(\bar{\nu}_R\nu_L + \bar{\nu}_L\nu_R)\ , \quad m_D = Y^\nu\frac{v}{\sqrt{2}}. \tag{7}$$

Where v is the vacuum expectation value of the Higgs field. The Dirac term conserves total lepton number but it can break the lepton flavor number symmetries.

The sum of the two mass terms can be written in matrix form

$$\mathcal{L}_{DM} = -\frac{1}{2}\begin{pmatrix}\bar{\nu}_L & \bar{\nu}_R^c\end{pmatrix}\begin{pmatrix}0 & m_D \\ m_D & M\end{pmatrix}\begin{pmatrix}\nu_L^c & \nu_R\end{pmatrix} + h.c. \tag{8}$$

The masses of the physical neutrino states will be the eigenvalues of the matrix above, which are:

$$m_\pm = \frac{M \pm M\sqrt{1 + 4m_D^2/M^2}}{2} \tag{9}$$

The eigenstates are:

$$\nu = \cos\theta(\nu_L + \nu_L^c) - \sin\theta(\nu_R + \nu_R^c) \tag{10a}$$

$$N = \cos\theta(\nu_R + \nu_R^c) + \sin\theta(\nu_L + \nu_L^c) \tag{10b}$$

Where $\tan\theta \approx m_D/M$. As we can see, the effect of the Majorana mass term is reducing the weak charged-current of light neutrino states by a $\cos\theta$ factor.

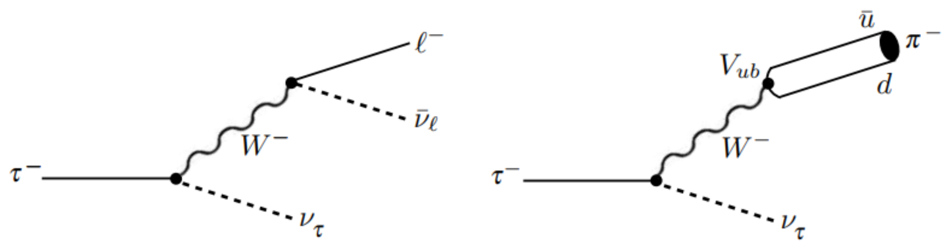

FIG. 3: Feynman diagrams to the tree level of leptonic (left) and hadronic (right) τ-lepton decays.

2.3.2. *The seesaw mechanism*

This seesaw limit [26–32] is defined as the limit where $M \gg m_D$. In this case, the eigenvalues from Eq. 9 become:

$$m_\nu = \frac{m_D^2}{M} \ , \quad m_N = M, \tag{11}$$

corresponding to the light (ν) and heavy (N) neutrino states. The seesaw mechanism actually explains why the light neutrinos are so light, and predicts the existence of the "heavy neutral leptons" (HNLs, signed with N) with mass of $m_N = M$. Under this limit, the final states from Eq. 10 becomes:

$$\nu \approx (\nu_L + \nu_L^c) - \frac{m_D}{M}(\nu_R + \nu_R^c) \tag{12a}$$

$$N \approx (\nu_R + \nu_R^c) + \frac{m_D}{M}(\nu_L + \nu_L^c) \tag{12b}$$

Hence, the light neutrino couples to the weak-charged current in the same way as the SM neutrinos. From the same reason, N is mostly RH (sterile), so it does not participate in any kind of weak interaction.

2.4. τ physics

As our search focuses on HNL in τ decays, some of the τ-lepton properties should be discussed. Like the other leptons, it interacts directly only via the weak interaction. However, τ is the only lepton that can decay into hadrons without violating mass-energy conservation, due to its relative high mass (m_τ =1.776GeV). Hence, the τ-lepton's decays can be divided into two types: leptonic or hadronic. Fig. 3 presents the simplest decay modes possible of these two types. Some of the most common decay modes and their branching fractions are presented in Table I. Note that "1-prong decay" means that the tau has only 1 charged daughter.

Decay mode of τ^-	Branching fraction
$\mu^-\bar{\nu_\mu}\nu_\tau$	17.39 ±0.04
$e^-\bar{\nu_e}\nu_\tau$	17.82 ±0.04
$\pi^-\nu_\tau$	10.82 ±0.05
$\pi^-\pi^0\nu_\tau$	25.49 ±0.09
1-prong decay	85.24 ±0.06

TABLE I: Common decay modes of τ-lepton

2.5. HNL model for this thesis

As declared before, the main goal of this thesis is to present our search for the HNL. In the naive seesaw mechanism presented above, the mixing coefficient is $V_{\ell N} \approx \sqrt{m_\nu/m_N}$. We are interested in $m_N \sim$ GeV, so with $m_\nu <$eV, this implies $V_{\ell N} < 10^{-4}$, making HNL production at colliders much too small to be observed. Therefore, all searches, including this one, rely on more complicated models, in which the value of $V_{\ell N}$ is independent of that of the HNL mass m_N. In these models, the SM neutrino can be written as a superposition of the ν and N mass states in the following way [33]:

$$\nu_L = \sum_{i=1}^{3} U_{\ell i}\nu_i + V_{\ell N}N \tag{13}$$

where $U_{\ell i}$ and $V_{\ell N}$ are the mixing parameters. We took $V_{\ell N} \ll 1$. This small mixing between LH neutrino and HNL, enables HNL production and decay in SM processes.

As mentioned in the Sec. 1, most previous researches utilized the mixing parameters with electrons and muons V_{eN}, $V_{\mu N}$. Our research focus on mixing with τ lepton and the parameter $V_{\tau N}$ under the assumption that $|V_{\tau N}| \ll |V_{eN}|, |V_{\mu N}|$, in which the N mixes mainly with the τ neutrino, and its mixing with the electron or muon neutrinos can be neglected. Therefore, it is advantageous to search the HNL in τ-decays, and the best place to that is at B-factories. B-factories are particle collider experiments designed to produce and detect a large number of B mesons via electron-positron collision, but they are also a significant source for $e^+e^- \to \tau^+\tau^-$ processes.

The decay rate of the process $\tau \to \pi N$ is obtained by replacing $N \to \tau$ and $\ell \to N$ in Eq.(3) of Ref. [34]:

$$\begin{aligned} Br(\tau^- \to N\pi^-) = \frac{G_f^2}{16\pi} f_\pi^2 |V_{ud}|^2 |V_{\tau N}|^2 m_\tau^3 \lambda^{1/2}\left(1, \frac{m_N^2}{m_\tau^2}, \frac{m_{\pi^-}^2}{m_\tau^2}\right) \\ \times\left[1 + \frac{m_N^2}{m_\tau^2} - \frac{m_{\pi^-}^2}{m_\tau^2}\left(1 + \frac{m_N^2}{m_\tau^2}\right) - 4\frac{m_N^2}{m_\tau^2}\right] /\Gamma_\tau \end{aligned} \tag{14}$$

Where G_f is Fermi coupling constant, m_{π^-} and m_N denote the mass of the charged pion and sterile neutrino, respectively; V_{ud} is the CKM matrix, f_π is the pion decay constant and Γ_τ is the τ lepton's decay rate; the function $\lambda(x, y, z)$ is defined as $\lambda(x, y, z) = x^2 + y^2 + z^2 - 2(xy + yz + zx)$.

The method that this thesis presents (and is discussed elaborately in the following sections), exploits the long lifetime of the low-mass N, which goes as [35]:

$$c\tau_N = 0.324 \text{ cm} \times \left(\frac{m_N}{1 \text{ GeV}}\right)^{-5.44} |V_{\tau N}|^{-2} \tag{15}$$

Particularly when produced at relativistic speeds, the N travels macroscopic distance inside the detector before decaying. The resulting displaced-vertex signature is particularly useful for suppressing background (see 6 6.2) [33].

3. EXPERIMENTAL SETUP

3.1. KEKB collider

KEKB [36] was an asymmetric electron-positron collider, which operated mostly at the center of mass energy of 10.58GeV, corresponding to the center-of-mass energy of $\Upsilon(4S)$ resonance. The CM frame is boosted due to the asymmetry in energies of the electron and the positrons. Other resonance states were also produced $\Upsilon(1S), \Upsilon(2S), \Upsilon(3S), \Upsilon(5S)$, as well as off-resonance states, which were set 60MeV bellow each of these on-resonance states. The collected data of the states is listed in Table II [37]. KEKB accelerated the electrons and the positrons in two different rings: the electrons in a High Energy Ring (HER) with 8GeV and the positrons in a Low Energy Ring (LER) with 3.5GeV. Each ring has a circumference of 3016m and is composed of four straight sections and four bends. The two rings are located side by side in the accelerator tunnel. KEKB layout is depicted in Fig.4. KEKB in particular, and e^+e^- colliders in general, are suitable for studying tau physics. τ leptons are produced in pairs through the following electroweak process: $e^+e^- \to \gamma/Z \to \tau^+\tau^-$. The cross section of this process for center of mass energy of the $\Upsilon(4S)$ is 0.919 ± 0.003 nb [38], what allowed the Belle detector to collect high number of 8.8×10^8 of $e^+e^- \to \tau^+\tau^-$ events [33].

Resonance state	On-resonance lumi. [fb^{-1}]	Off-resonance lumi. [fb^{-1}]
$\Upsilon(1S)$	5.7	1.8
$\Upsilon(2S)$	24.9	1.7
$\Upsilon(3S)$	2.9	0.25
$\Upsilon(4S)$	711	89.4
$\Upsilon(5S)$	121.4	1.7

TABLE II: Summary of luminosity integrated by Belle

3.2. Belle detector

The Belle detector was installed in the Tsukuba hall, where the accelerated particles collide. The position at which the particles' beams cross is called interaction point (IP). The detector's purpose is to detect the particles that are produced in this collision. The Belle detector was about 3.6π solid angle composite detector with rotational symmetry

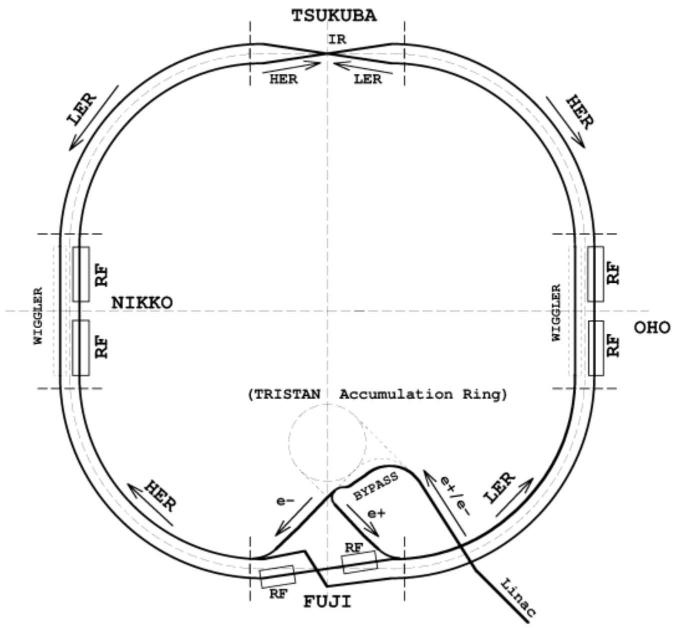

FIG. 4: Schematic layout of KEKB accelerator complex

around the beam axis. It was, however, asymmetrical in the forward-backward direction due to the asymmetry of energy between the electron and positron beams.

The Belle detector [39] was designed with multiple layers, going inside-out, similarly to other particle detectors. Belle had a different types of a sub-detectors, and all together gave detailed information about the collision event. Some of the information is used for particle identification, which is provided to us by the reconstruction software (see Secion 3 3.3 for more details about the software framework) as the parameter **particle ID (PID)**. PID is a likelihood function that gives the degree of confidence that the particle is really the particle related to the PID (eID is the function for electrons and muID for muons). This distribution is calculated based on the information achieved by different components of the detector, which are described in the following paragraphs. Fig. 5(6) presents the eID (muID) distribution of an electron (muon) and a non-electron (non-muon) particle, in this case a pion.

The sub-detectors are shown in Fig.7, and, and their roles are described as follows, going from the inner part of Belle outside:

- **SVD – Silicon Vertex Detector**: The SVD is located outside the cylindrical beryllium beam pipe, which holds the vacuum needed for the beams. Its purpose is to measure the z-axis vertex position of the τ, B and D mesons, with the best possible resolution. Information from the SVD is used for PID estimation. Two different SVDs were used during the experiment. The first one, named SVD1, had 3 layers (30, 45.5, 60.5 mm radii) in a barrel-only design and covered an angle of $23° < \theta < 139°$, corresponding to 86° of the full solid angle, where θ is the angle from the beam axis (polar angle). Afterwards, SVD1 was replaced by SVD2 due to radiation damage. SVD2 consisted 4 layers (20, 43.5, 70 and 88 mm radii) and covered $17° < \theta < 150°$. This is the closest the SVD can be installed to the beam pipe, since a double-wall beryllium

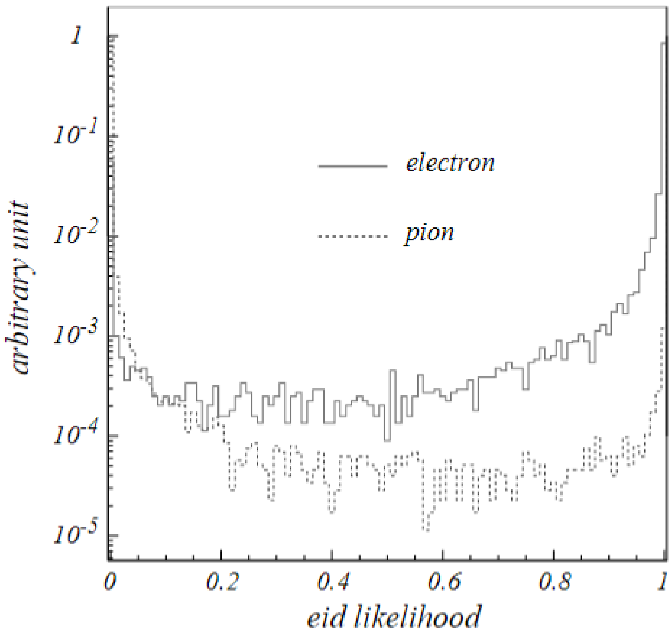

FIG. 5: eID likelihood distributions for electrons (solid line) and for pions (dashed line). [40]

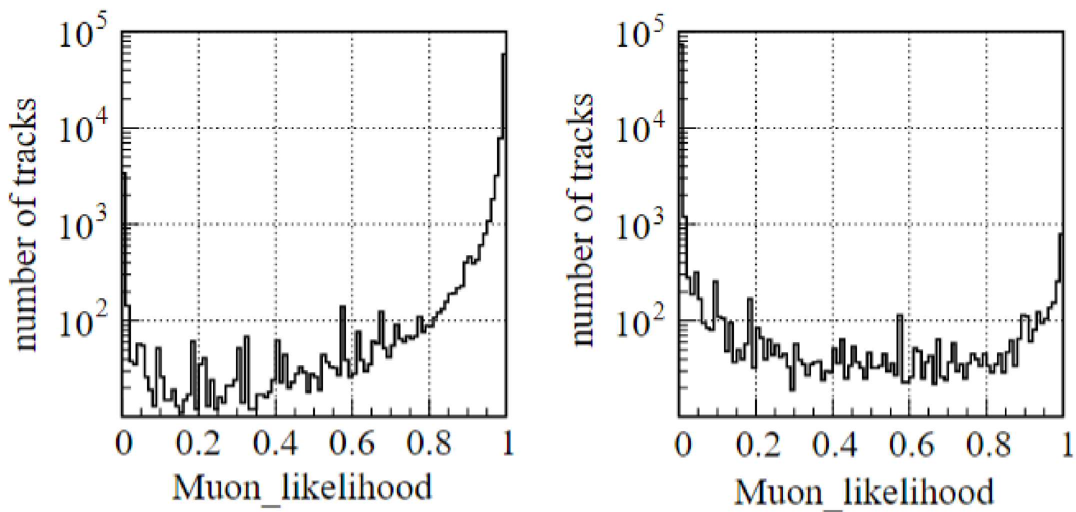

FIG. 6: muID likelihood distributions for muons (left) and for pions (right). [40]

cylinder with an inner diameter of 40 mm is built around the pipe, used as a shielding mechanism for the SVD.

- **CDC – Central Drift Chamber**: The CDC is a component of great importance for charged particles reconstruction, which includes tracking, momentum measurement and particle identification via energy loss (dE/dX) measurement. The momentum measurement exploits the magnetic field of a super-conducting solenoid of 1.5T, which resides between the ECL and the KLM. The inner and outer radii of the CDC are 103.5

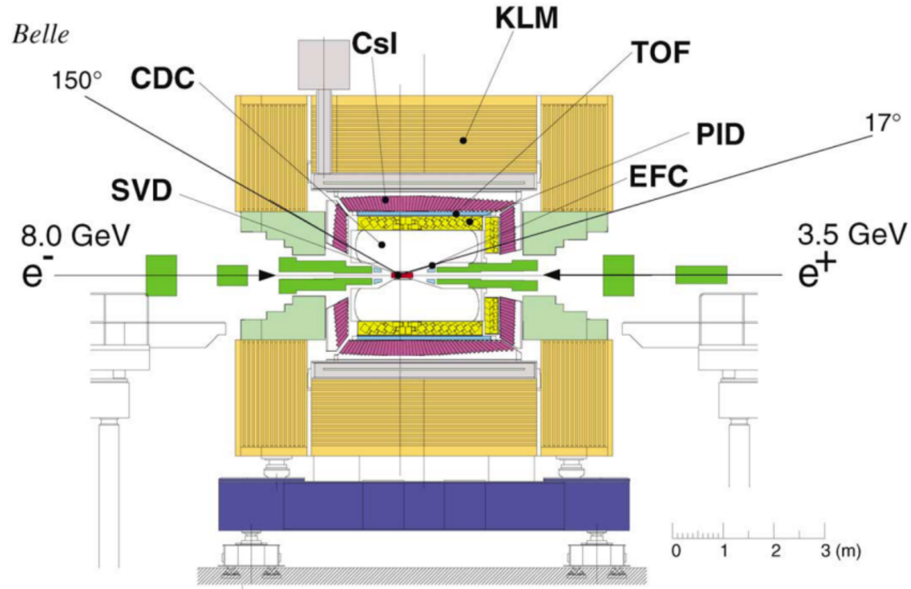

FIG. 7: Schematic layout of Belle detector [39]

mm and 874 mm, respectively. The structure of the CDC is of great importance for the understanding of the selection cuts we apply in Sec 6, so its overview is presented in Fig. 8.

The CDC has 8400 drift cells in 50 cylindrical layers. Most of the drift cells are almost square and have a drift distance between 8 and 10 mm. Each cell is formed by a grid of field wires and a sense wire. As a charged particle moves through the drift cell, it ionizes the gas. The field wires are negative and the sense wire is positive, so that the electrons from the ionization drift under the electric field toward the sense wire. When they get very close to the sense wire, the field (which goes like $1/r$) is so large that the electrons gain enough kinetic energy during their mean free path that they ionize more electrons, which ionize more electrons etc., until all the ionized electrons reach the sense wire and are collected there. This avalanche yields a signal amplification of order 10^4 and reduces the need for strong electronic amplification of the signal.

The transverse momentum resolution for charged particles with $p_t \geq 100 MeV/c^2$ is $\frac{\sigma_{p_t}}{p_t} \sim \%0.3\sqrt{1+p_t^2}$ (p_t in GeV/c) in the polar angle region of $17° < \theta < 150°$ (the CDC is asymmetric in the z-axis). This high resolution above is achieved by low-Z gas (50% helium, 50% ethane mixture), in order to reduce multiple scattering.

- **ACC – Aerogel Cherenkov Counter system**: The main functions of the ACC are distinguishing $\pi^{\pm}$ and $K^{\pm}$ mesons, extending the momentum coverage for particle identification beyond the reach of dE/dx measurements in the CDC and time-of-flight measurements in the TOF. When charged particles travel with velocity v higher than the speed of light in a dielectric medium of refractive index n ($v > c/n$) in the material, they emit radiation called "Cherenkov light". This radiation is emitted at an angle given by $\cos\theta = 1/(\beta n)$, where $\beta \equiv v/c$. For beta too small, $\cos\theta > 1$ which means that there is no radiation. The value of n is chosen such that for most of the

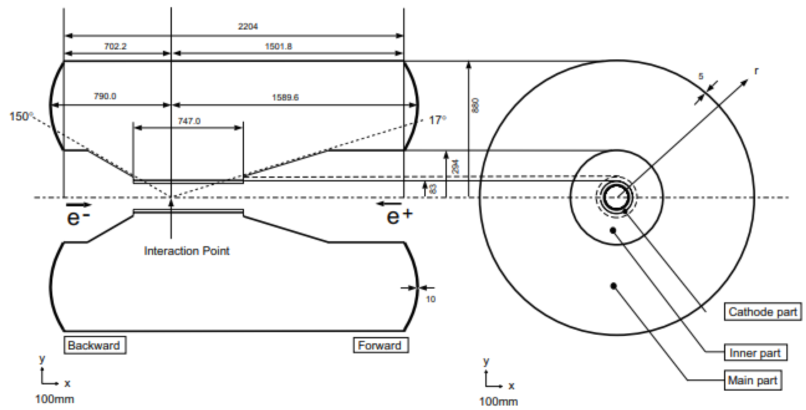

FIG. 8: Schematic layout of CDC

momentum range of interest, pions emit Cherenkov light while kaons don't, since their β is too slow. The silica aerogels that is used as the radiators in the ACC have a refractive indices between 1.01 to 1.03. The ACC consists of 960 counter modules for the barrel part and 228 modules for the forward end-cap part of the detector. One or two fine mesh-tubes photo multiplier tubes (FM-PMT) are used per module, for detection of the Chenekov light. The FM-PMT are attached directly to the aerogel for that purpose.

- **TOF – Time of Flight detection system**: The TOF system is composed of plastic scintillation counters which are used as an additional tool for particles identification. The TOF has a 100ps time resolution and is situated such that hard particles have a flight path of 1.2m, which makes this system effective for particle momenta below about 1.2 GeV/c. The TOF is also utilized for providing fast timing signals for the trigger system. The TOF system includes 128 counters and 64 trigger scintillation counters (TSC), which are divided to 65 modules located at a radius of 1.2m from the IP. The system polar angle coverage is $34° < \theta < 120°$. The counters of both types use FM-PMTs for their scintillation counting operation.

- **EFC – Extreme Forward Calorimeter**: The EFC is installed in order to extend a polar angle area, which otherwise wouldn't be covered by the electromagnetic calorimeter (ECL): $6.4° < \theta < 11.5°$ in the forward direction, and $163.4° < \theta < 171.2°$ in the backward direction. Additional role the EFC plays is being used as a beam mask, reducing the background in the central drift chamber (CDC). It is also used for monitoring the beam and the luminosity of Belle. For the sake of this goals, the EFC is installed in the front faces of the cryostats of the compensation solenoid magnets of the KEKB accelerator, surrounding the beam pipe. To withstand the high radiation near the interaction point, the EFC is made of Bismuth Germanate (BGO, $Bi_4Ge_3O_{12}$). Its energy resolution is:
$$\frac{\sigma_E}{E} = \frac{(0.3-1)\%}{\sqrt{E[GeV]}} \tag{16}$$

- **ECL – Electromagnetic Calorimeter**: The ECL is the main tool in the detector for detection of photons (which are charge-less particles, hence undetectable in the CDC) and for measuring their energies. The photons that the ECL detects are high-energy photons that come mostly from π^0 decays, but also other sources. Such a photon creates an EM shower in the ECL. The energy of most photons in Belle is below 500 MeV, what makes the performances of the ECL in this energy range very important. The ECL in Belle consists of 8736 CsI(Tl) crystals with a silicon photodiode readout. This type of crystal was chosen due to its important features e.g. high photon yield, weak hygroscopicity and mechanical stability.

The ECL has a barrel section of with a length of 3.0 m and an inner radius of 1.25 m, and annular end-caps at $z = +2.0m$ and $z = -1.0$ from the IP. The polar angular coverge of this system is $17° < \theta < 150°$.

- **KLM – K_L^0 and μ detector**: This sub-dector is responsible for identification of muons and of K_L^0 mesons. The muon identification is done only for candidates with a momentum greater than 600 MeV/c. Otherwise, they either don't reach or done penetrate the KLM deep enough to leave a clear muon signal. For K_L there is no such momentum limit.

  The polar angular coverge of this system is $20° < \theta < 155°$ (including barrel part and endcap parts). The KLM is divided to 15 layers of charged-particle detectors and to 14 iron layers in each the octagonal barrel region. Moreover, there are 14 detector layers in each of the forward and backward end-caps. Between each layer, there is an RPC (resistive plate chamber) detectors to detect the muons that pass through from the absorber layers.

  The μ (K_L^0) detection is done by observing clusters in the KLM which are (not) associated with charged tracks in the CDC. The multiple layers of charged particle detectors and iron allow the discrimination between muons and charged hadrons, as muons travel much farther with smaller deflections on average than strongly interacting hadrons. As for the K_L^0, they interact hadronically and produce a shower of ionizing particles in the ECL or the iron. The location of this shower determines the direction of the K_L^0 (fluctuations in the size of the shower prevent a useful measurement of the energy).

- **Detector solenoid and iron structure**: The superconducting solenoid induces a magnetic field of 1.5 T. The solenoid has a diameter of 3.4 m and a length of 4.4 m. The iron yoke surrounding the magnet has several functions. First, it is used as a return path of the magnetic flux. Second, it serves as the absorber material for the KLM. The iron yoke's components masses are 608 tons for the barrel yoke and 524(2x262) for the end-cap yokes.

3.3. Analysis software framework

Fig. 9 displays the workflow for both real data and Monte-Carlo (MC) simulation processes from the starting point (which is different for real data and MC) and up to the final samples that will be used for offline analysis. The data was collected from the Belle detector's measurements. The specific data samples that we use are elaborated in Sec. 5. The MC is generated with the number of appropriate generators. Each generator knows how to generate the physics for particular processes. The generators and the corresponding

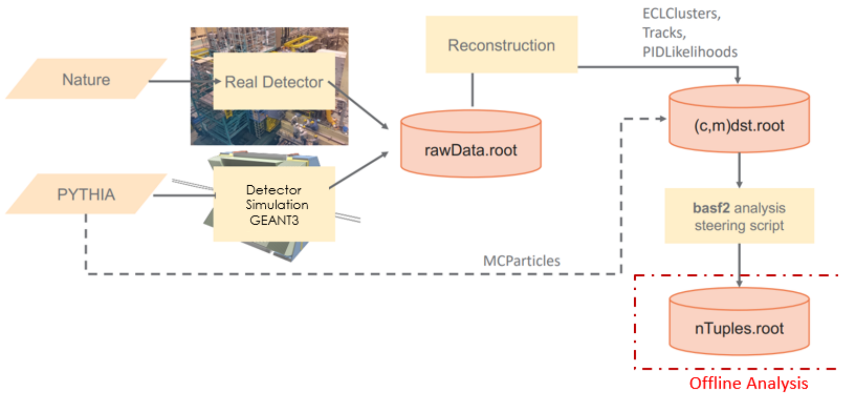

FIG. 9: Data and MC schematic process tree

processes are elaborated in Sec. 5 5.2. The outcome of the generators' work is a list of particles with mother-daughter relations, 4-momenta, and production positions. This is then fed into a GEANT3 simulation of the particle's interactions with the detector material and the electronic response of the detector. The electronic response output has the same format (channel for channel) as the real data that's obtained from the detector.

Afterwards, both data and MC samples need to be processed from raw-data configuration to a data-format which will eventually includes the reconstructed tracks, 4-momenta of the each detectable particles and additional essential parameters (e.g. PID and decay vertices). This format is called an "ntuple". All these steps demand an efficient and reliable software.

Such software is Belle Analysis Framework (`basf`) [41], which is the software framework intended for generation, reconstruction and analysis of Belle events. Eventually, we preferred to use the software for Belle II (`basf2`), because it is more updated and includes more useful features. In Sec. 5 5.2 we explain where we use each one. When we used basf for MC generation processes, we then converted the output files of basf to basf2 output format file, with a package in basf2 called `b2bii` [42].

The work of basf2 is implemented with processing blocks called *modules*, each executing a defined task. A sequence of modules creates a *path*. When a path is processed, the modules it includes are executed in order.

For our final limit plots of $V_{\tau N}$, we use pyhf [43, 44], which a python implementation of the HistFactory framework [45]. HistFactory is a tool to build parametrized probability density functions (p.d.fs) based on simple ROOT histograms organized in an XML file. Although the p.d.f has a restricted form, it is able to describe various analyses based on template histograms. The tool takes a modular approach to build complex p.d.fs from more primitive conceptual building blocks. See Sec. 10 for more explanation about the p.d.f and the way we use it.

4. ANALYSIS METHOD OVERVIEW

This analysis probes directly $V_{\tau N}$, the coupling of the HNL and τ lepton. It is done by searching for HNL production via $\tau^- \to N\pi^-$ following the method of Ref. [33].

This production mechanism implies $m_N < m_\tau - m_\pi$. Further restricting ourselves to the scenario in which the HNL mixings with the ν_e and ν_μ are negligible, we see that the HNL can decay only via the weak neutral current to $Z^*\nu_\tau$. In this analysis we consider only the $\mu^+\mu^-$ final state of the Z^*. The branching fractions $Br(\tau^- \to N\pi^-)$, $Br(N \to \mu^+\mu^-\nu_\tau)$, and the HNL lifetime are taken from Ref. [46], and they are tabulated in Appendix C

We reconstruct $e^+e^- \to \tau^+_{tag}\tau^-_{sig}$ in which the τ^+_{tag} undergoes a 1-prong decay. The signal decay is $\tau^-_{sig} \to \pi^- N$ followed by $N \to \mu^+\mu^-\nu_\tau$. The Feynman diagram corresponding to the signal τ decay is shown in Fig. 10.

Due to Eq. 14 and 15, $V_{\tau N}$ impacts both the number of signal events produced and the lifetime. Therefore, the range of $V_{\tau N}$ that the analysis is sensitive to is governed by both of these properties. It so happens that this range is such that the HNL is long lived, as will be shown later. Because HNL lifetime, the $\mu^+\mu^-$ form a displaced vertex (DV). To suppress background from promptly produced tracks, K_S and Λ decays, and particle interactions in dense material, the radial position r_{DV} of the DV is required to satisfy $r_{\mathrm{DV}} > 15cm$. This tight cut implies that the analysis focuses on small values of the squared mixing parameter $|V_{\tau N}|^2$ between the HNL and the SM neutrino.

The decay chain cannot be fully reconstructed, due to the unobservable neutrino in the final state. There are 12 unknowns, namely, the 4-momenta $p^\mu_{\nu_\tau}, p^\mu_N, p^\mu_\tau$ of the unreconstructed ν_τ, N and τ respectively. However, the decay chain has 12 constraints: 4-momentum conservation in the τ and N decays (8 constraints), the known masses of the τ and the ν_τ (2 constraints), and the unit vector from the production point of the π system to that of the $\mu^+\mu^-$ system, which is the direction of $\vec{p}_N$ (2 constraints). Solving the constraint equations, one determines the 4-momenta of all the particles up to a two-fold ambiguity arising from a quadratic equation. [33]. The calculation is shown in detail in Appendix A.

The resulting two HNL-mass solutions are referred to as m_+ and m_-, depending on the sign in front of the term $\sqrt{A_{\mathrm{sq}}}$, which arises from a quadratic equation. Due to the very low background, a detailed fit of the m_+ vs. m_- distribution is not needed. Rather, we use only a course cut on these variables in one of the signal regions (see Sec. 6). Ref. [33] also suggests exploiting the signal-τ CM-energy solutions $E_\pm$ for additional background suppression. As the plots presented below demonstrate, given the low background there is no particular advantage in using $E_\pm$.

After event selection, the final statistical analysis is performed with `pyhf` in 2 signal regions, SRHeavy and SRLight which target light and heavy HNLs in low-background large-radius region of the detector. The fit background model is obtained from MC, and data control regions (CRs) are used in the fit to determine the background level in the SRs.

A comparison between the $V_{\tau N}$ bound set by DELPHI, to the expected $V_{\tau N}$ bound from Belle (and other future experiments), using the method offered by Ref. [33], is presented in Fig. 11.

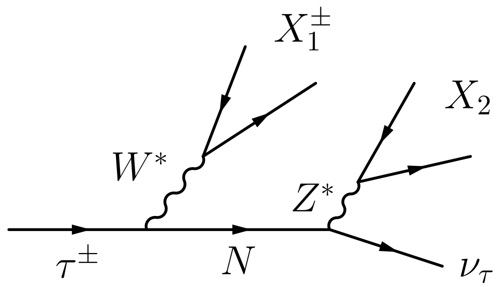

FIG. 10: The decay chain searched for in this analysis, with $X_1 = \pi^\pm$ and $X_2 = \mu^+\mu^-$.

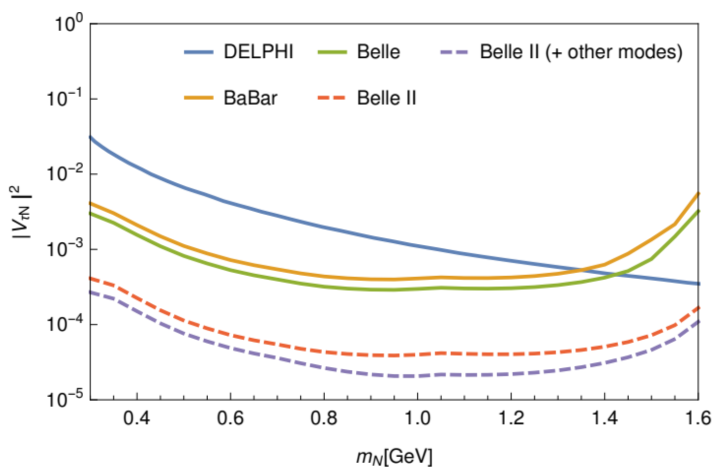

FIG. 11: Expected 95% confidence-level limits on the coupling $V_{\tau N}$ vs m_N, obtainable from the decay chain described in Fig. 10 with $X_1 = \pi^\pm(\pi^0)$ and $X_2 = \ell^+\ell^-$, between the different experiments. Also shown is the potential impact of adding the modes $X_1 = \ell\nu$ and $X_2 = \pi^+\pi^-$

.

5. DATA AND MONTE-CARLO SAMPLES

5.1. Data samples

The analysis uses data taken from the period of time during the Belle experiment operation. The events of the above data-set passes tau_skimB, which is a collection of high-level analysis scripts that reduce the data set to a manageable size by applying a simple selection. The exact conditions are presented in in Table III. The data samples have an integrated luminosity of 702.623/89.454 fb^{-1} for events on/off-resonance $\Upsilon(4S)$, and 121.061/1.73 fb^{-1} for events on/off-resonance $\Upsilon(5S)$, respectively. Currently, the data is still blinded, so the data analysis has not been done yet, but only the MC. An internal belle review committee has been formed for examining the analysis and giving an approval for unblinding of the data.

Index	Tauskim criteria
1	$2 <$ Number of charged tracks < 8
2	Sum of charge: $\lvert q_{\rm sum} \rvert \leq 2$
3	Maximum p_T of charged track, $p_T^{\rm max} > 0.5$ GeV
4	Event vertex: $\lvert dr \rvert < 1.0$ cm and $\lvert dz \rvert < 3.0$ cm
5	For two-track events, 5-a and 5-b must be satisfied.
5-a	$E_{\rm ECL} < 11$ GeV
5-b	$5^\circ < \theta_{\rm miss} < 175^\circ$
6	$E_{\rm rec} >3$ GeV or $p_T^{\rm max} > 1$ GeV
7	For 2-4 track events, 7-a and 7-b must be satisfied.
7-a	$E_{\rm tot} < 9$ GeV or $\theta^{\rm max} < 175^\circ$ or $2 < E_{\rm ECL} < 10$ GeV
7-b	$N_{\rm barrel} \geq 2$ or $E_{\rm ECL}^{\rm trk} < 5.3$ GeV

TABLE III: Selection criteria included in tauskim package; dr and dz are defined in Sec. 6 6.1, E_{ECL} is the total energy measured in the ECL, θ_{miss} is the polar angle of the missing momentum, E_{rec} is the sum of the total momenta of good charged tracks and gamma energy in CM frame, E_{tot} is the sum of E_{rec} and the missing momentum in CM frame; N_{barrel} is the number of tracks in the barrel region.

5.2. MC samples

To study the effect of the selection criteria and the performance of the fits, Monte Carlo (MC) samples are used. These MC simulate the production and decay of variety of particles and their interactions with the matter inside the detector. These MC samples are divided into two types: generic MC and signal MC. The goal of the generic MC is to simulate the background process as best as we can, and it is used to study the background. We use run-dependent generic Monte-Carlo samples which pass the tau skim criteria and trigger simulation. Belle's MC is divided into streams, where each stream of simulated events corresponds to the number of events in the recorded data sample for a given decay type. The details of the samples used are summarized in Table IV

In signal simulates the signal we are searching for. We generate experiment-dependent signal $\tau_{sig}^- \to \pi^- N(\to \mu^+\mu^-\nu_\tau)$ MC using `KKMC` [48] and `PYTHIA` [49] event genrators. `KKMC` is used for generating the process $e^+e^- \to \tau_{tag}^+\tau_{sig}^-$ (including initial/final stater radiation). `PYTHIA` is used for the generating the τ and HNL decays. The samples are generated in the BASF2 framework and the detector simulation is performed in the BASF framework. Table V lists the values of the N mass m_N and lifetime $c\tau$ and the number of events generated for each sample. The lifetime values are chosen so as to yield a reasonably large number of events in the fiducial volume of the analysis (see Sec. 6) to enable high-statistics determination of the signal efficiency (see Sec. 7).

Process (production of e^+e^- collision)	$\Upsilon(4S)$ Lumi (fb^{-1}) On/Off	$\Upsilon(5S)$ Lumi (fb^{-1}) On/Off	Streams
$\tau^+\tau^-$	702.623/89.454	121.061/1.73	5
$\mu^+\mu^-$	702.623/89.454	121.061/1.73	5
Bhabha	51.924/5.085	0/0	5
$e^+e^-e^+e^-$	455.294/58.121	0/0	3
$e^+e^-\mu^+\mu^-$	455.294/58.121	0/0	3
$eeqq(q = u, s, c)$	62.615/72.806	0/0	5
uds	702.623/89.454	121.061/1.73	5
charm	702.623/89.454	121.061/1.73	5
B^+B^-	702.623/00.000	121.061/00.00	5
$B^0\bar{B}^0$	702.623/00.000	121.061/00.00	5

TABLE IV: Generic MC samples for different processes and their corresponding luminosities per stream used in this analysis. The numbers of streams used for different processes are summarized as well. [47]

m_N (GeV)	Generated events	$c\tau$ (cm)
0.3	1479720	15.0
0.4	1447884	15.0
0.5	1398591	15.0
0.6	1457528	22.5
0.7	1470659	22.5
0.8	1468197	22.5
0.9	1464336	22.5
1.0	1460280	22.5
1.1	1453751	30.0
1.2	1447480	30.0
1.3	1437136	30.0
1.4	1422052	30.0
1.5	1398034	30.0
1.6	1369152	30.0

TABLE V: Signal MC samples generated for different masses and lifetimes of N. The differences between the numbers of events are due to some crashed jobs.

6. EVENT SELECTION

We have online selection used to produce ntuples for offline processing, where events are further selected using the ”offline” selection.

6.1. Online event selection

The application of the cuts is divided into 3 different steps: primary cuts, vertex-fitting and final cuts.

6.1.1. Primary online selection criteria

The selection of primary tracks and neutral particles through the online selection criteria are designed for rejecting most of the non-$\tau\tau$ backgrounds. We look for a topology in which one track is roughly back-to-back with 3 additional tracks, as was discussed in Sec.4. The former is the "tag-side" (related to τ_{tag}) and the last is the "signal-side" (related to τ_{sig}).

Our primary selection criteria are described as follows:

- Track-quality selection: All tracks must have at least 20 CDC hits. In addition, we want to assure that the signal-side pion and the tag-side track really originated from the two taus, i.e. the tracks are close enough to the IP. For this goal, we use the variables $|dr|$ and $|dz|$, which are defined as the distance between the IP and point of closest approach (POCA) to the IP of the tracks, in the r and z axis correspondingly. We select only events that satisfy $|dr| < 0.5\,\mathrm{cm}$, $|dz| < 2.0\,\mathrm{cm}$.
- Signal side muon selection: the muon ID has to be muID>0.5.
- Signal side pion selection: no particle-ID cut.
- Tag side 1-prong: no particle-ID cut.

6.1.2. Vertex-fitting

The m^+ and m^- daughters of signal HNL candidates that satisfy the above cuts, are vertex-fit with the `treeFitter` algorithm [50–52] to produce the DV. Vertex fitting is a technique in which one uses prior knowledge on the nature of a decay, namely, that the two muons are supposed to originate from the same point. This, in order to find the DV, so we can use it to select signal.

`treeFitter` is the standard basf2 module for fitting a full decay chain simultaneously. It performs a progressive fit, using a Kalman filter algorithm [53]. This algorithm input is the measured 4-momenta of final states particles, and their masses which is given as a constraint. The output of `treeFitter` gives an optimised fit with a χ^2 minimisation for the 4-momentum and the position of the vertex. [41]

The tracks are combined to reconstruct long-lived particle (N) with various final states as mentioned above. The N is combined with one pion to reconstruct the signal-side τ lepton. The tag-side τ lepton is reconstructed from a single charged lepton without applying any particle identification criteria.

6.1.3. *Last online selection criteria*

We define several selection regions with different purposes:

- The event selection for signal regions SRHeavy and SRLight is intended to suppress the reducible backgrounds while maintaining a high signal efficiency. The difference between the two regions is that SRHeavy targets heavy HNLs and SRLight targets light HNLs. The control regions CRHeavy (target heavy HNL) and CRLight (targets light HNL) are used to determine the background in SRHeavy and SRLight, respectively. The main feature of the CRs is that one of the tracks in the DV is required to be a muon and the other is required to not be a lepton (electron or muon), so that it is almost always a pion. This choice is motivated by the presence of backgrounds from $\tau \to K_L \pi\nu$,$\tau \to K_L \pi\nu$ and $\tau \to 3\pi\nu$, with 1 or 2 pions undergoing decay in flight to a muon or a hard scatter and mis-dentification as a muon, as well as pions from $e^+e^- \to q\bar{q}$ events. This is in contrast to the 2-muon DV selection in the SRs.
- We have 5 validation regions (VRs) which are used for data-MC comparison:
  - The selection for the same-charge validation regions VRHeavySameSign and VRLightSameSign is identical to those of SRHeavy and SRLight, except that the two DV tracks are required to have the same electrical charge. (2 VRs)
  - The VRHeavy$\pi\pi$ and VRLight$\pi\pi$ in which we require both DV daughters to be non-leptons (so that they are almost always pions), but outside the K_S mass region. (2 VRs)
  - The K_S validation region VRK_S contains $\tau \to \pi K_S$, $K_S \to \pi^+\pi^-$ decays. (1 VR)

After the online selections, we have the reconstructed vertices of the decay chain, so additional cuts can be applied on their parameters. This cuts are the following:

- The radial position of the DV must satisfy $r_{\text{DV}} > 5$ cm. This reduces the sample size with a cut that is much looser than the one applied offline.
- The invariant mass $m(\pi + DV)$ of the prompt pion plus the DV must be smaller than the τ mass m_τ =1.776 GeV, to quickly reject obviously irrelevant candidates (we search in τ decays).
- The event is divided into two hemispheres centered on the event thrust axis [54], calculated with the observed tracks and photons. The three signal-side tracks are required to be in one hemisphere, and the tag-side single track is required to be in the other hemisphere. This is a standard 1-3 prong selection cut.

6.2. Offline signal region selection

Events that satisfy the online cuts are required to satisfy also the following offline cuts:

0. $\boldsymbol{N_{\text{tracks}}}$**:** The number of tracks in the event must be $N_{\text{tracks}} = 4$. This strongly suppresses hadronic ($q\bar{q}$ and $B\bar{B}$) background.

1. **r_{DV} cut:** The decay position of the HNL in the xy plane needs to satisfy $r_{\mathrm{DV}} > 15$ cm. This suppresses background from prompt particles (particularly those that undergo large-angle multiple scattering in dense material or decay in flight), as well as K_S and Λ decays.

2. **$P(\chi^2)$ cut:** The χ^2 probability of the DV fit is required to be $P(\chi^2) > 0.00001$. This ensures consistency of the DV fit.

3. **$\cos\theta_{\mu^+\mu^-}$ cut:** Cosine of the angle between the 2 muons must be $\cos\theta_{\mu^+\mu^-} > 0.5$. This selects tracks consistent with originating from a boosted parent.

4. **Prompt π L_{ID} cut:** The muon ID and electron ID of the prompt π are both required to be less than 0.01. This ensures pion selection and rejects background from QED events, particularly 4-lepton final states.

5. **CDC Hits min cut:** Each HNL-daughter muon needs to satisfy $r_{\mathrm{hit}} - r_{\mathrm{DV}} > -2$ cm, where r_{hit} is the radial position of the lowest-radius CDC hit on the track. This very loose cut rejects prompt tracks, for which there are hits at a smaller radius than r_{DV}.

6. **μ_{ID} cut 1:** The muon ID of at least one HNL-daughter muon must be greater than 0.9.

7. **K_S^0 veto:** The DV mass calculated with the pion mass hypothesis for the two DV daughters, is not in the range of $0.42 < m_{\pi\pi}^{DV} < 0.52$ GeV. This suppresses K_S^0 background, which is also a long-lived neutral particle, which can produce a DV similarly to the HNL.

8. **$\sum E_\gamma$ cut:** The total lab-frame energy of photons in the event must be less than 1 GeV, in order to reduce $q\bar{q}$ background (τ decays usually do not include high energy photons).

9. **E_{π^0} cut:** The lab-frame energy of any π^0 in the signal hemisphere must be less than 0.1 GeV. This suppresses background from, e.g., $\tau \to \pi\pi^0 K_S \nu$, given that we are not searching for $\tau \to \pi\pi^0 N$ signal.

10. **A_{sq} cut:** The argument A_{sq} of the square root in the HNL mass calculation Eq. A16 is required to be $A_{\mathrm{sq}} < 0.4 GeV$. This takes advantage of the fact that background tends to have larger values of A_{sq}.

11. **μ_{ID} (N) cut 2:** Muon ID of both muons (the two HNL daughters) must be greater than 0.9.

12. **Final $m_{\pi\pi}^{DV}$ and $m_\pm$ cuts**: these cuts define two signal regions that target heavy and light HNLs:

    - Signal region **SRHeavy**: $\boldsymbol{m_{\pi\pi}^{DV} > 0.52}$ **GeV**.
      This cut is efficient for heavy HNLs and rejects light HNLs. E.g., it is obvious that an HNL with $m_N < 0.52$ GeV cannot satisfy this cut.
    - Signal region **SRLight**:
        - $\boldsymbol{m_{\pi\pi}^{DV} < 0.42}$ **GeV**.
          This cut is efficient for light HNLs.

– $\boldsymbol{m_+, m_-}$ cut: either $m_+ < 0.9$ GeV or $m_- < 0.6$ GeV. This takes advantage of the fact that background events that satisfy $m_{\pi\pi}^{DV} < 0.42$ GeV tend to have high values of $m_\pm$, in contrast with signal.

The distributions of the cut variables for signal and for the $\tau\tau$ and $q\bar{q}$ backgrounds (which are by far the dominant background sources) in MC are shown in Figs. 12, 13, and 14. Each variable is presented before the associated cut is applied on the samples. All the distributions are normalized to the same area in order to compare them properly.

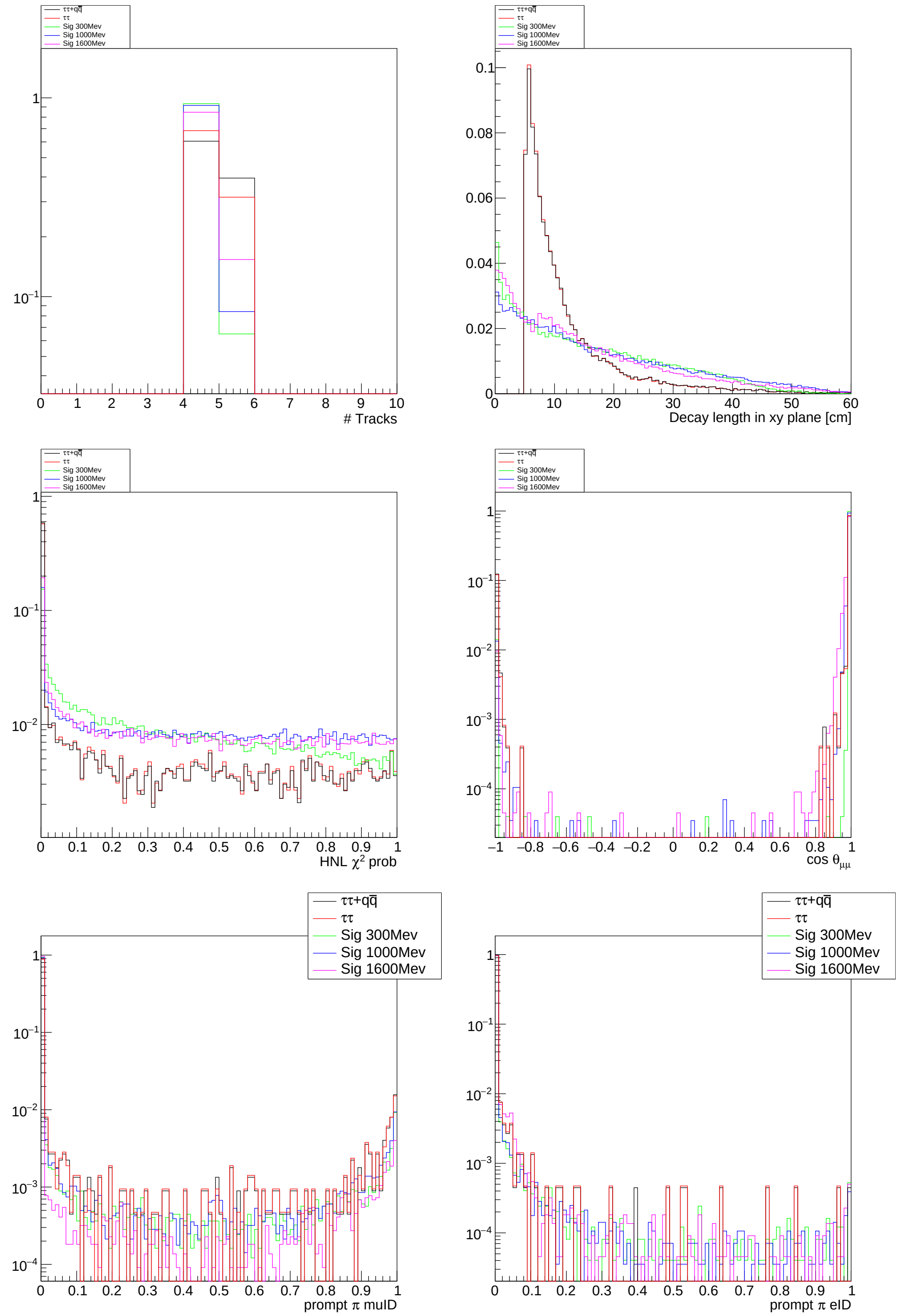

FIG. 12: Signal- and background-MC distributions for the number of tracks for 5 different samples (top left), r_{DV} after the N_{tracks} cut (top right), the χ^2 probability of the DV after the r_{DV} cut (middle left), cosine of the angle between the 2 muons after the $P(\chi^2)$ cut (middle right), μ-ID of prompt pion (bottom left), e-ID of prompt pion (bottom right); all histograms are normalized to the same area.

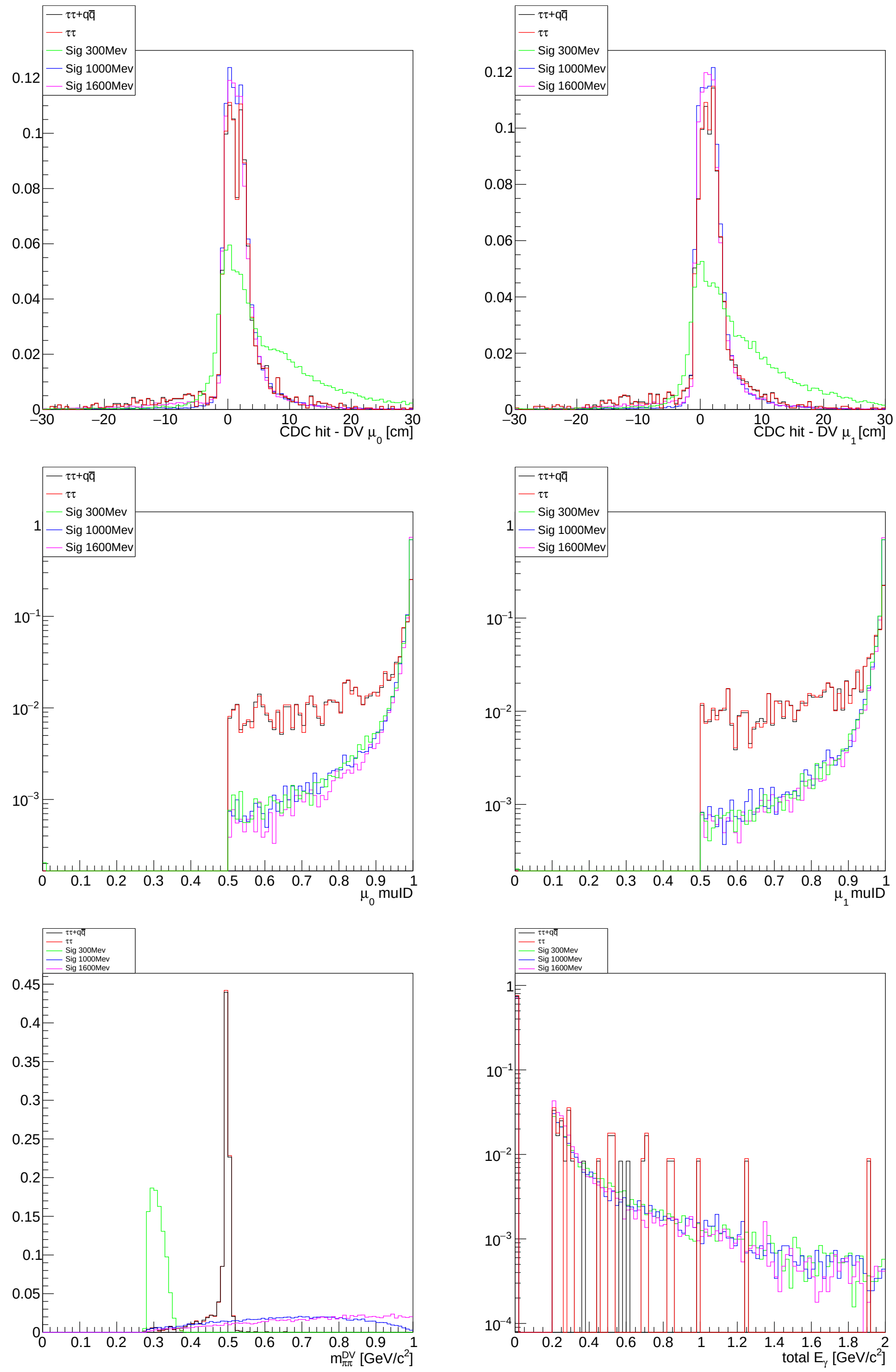

FIG. 13: Signal- and background-MC distributions for the difference between CDC hit position of μ_0 and HNL DV (top left), Difference between CDC hit position of μ_1 and HNL DV (top right), μ-ID of μ_0 (middle left), μ-ID of μ_1 (middle right), invariant mass of HNL daughters with pion mass hypothesis applied (bottom left), $\sum E_\gamma$ distribution (bottom right); all histograms are normalized to the same area.

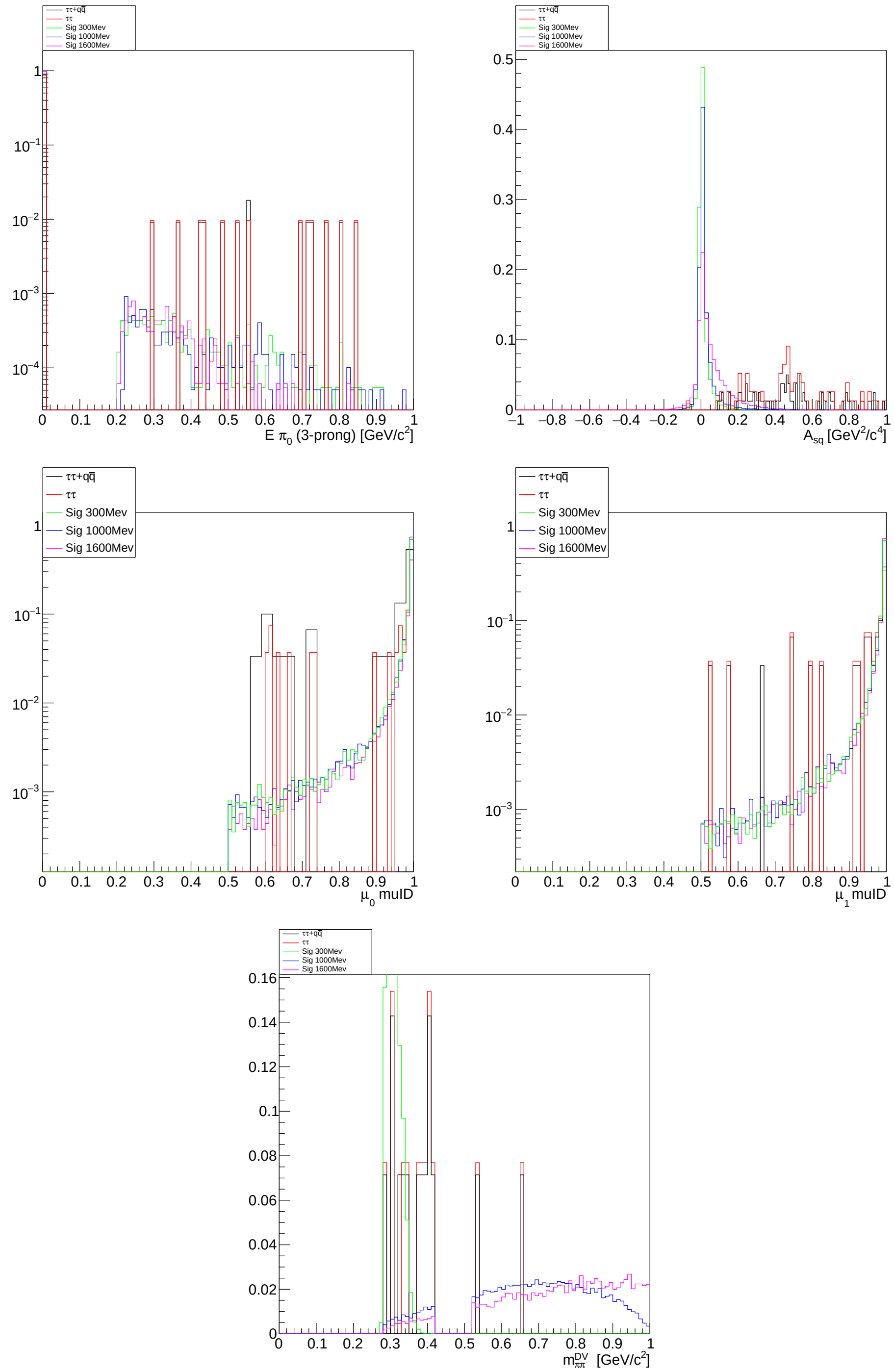

FIG. 14: Signal- and background-MC distributions for the E_{π^0} distribution (top left), $A_{\rm sq}$ distribution (top right), μ-ID of μ_0 (middle left), μ-ID of μ_1 (middle right), invariant mass of HNL daughters with pion mass hypothesis applied (bottom left); all histograms are normalized to the same area.

The number of MC events that pass each cut are shown in the cut-flow Table VI for the generic backgrounds and for three representative signal samples, generated with HNL masses of 300, 1000, and 1600 GeV - see Sec 5 5.2 For each cut, Table VI also shows the total expected number of background events in the data and the MC-statistical uncertainty on this number. These values constitute the background model for the pyhf fit.

The third-last (last) row in Table VI corresponds to the final cuts of SRHeavy and SRLight. From these rows, we see that the expected numbers of background events in these SRs are

$$\begin{aligned} N^{MC}_{SRHeavy} &= 0.40 \pm 0.28, \\ N^{MC}_{SRLight} &= 0.80 \pm 0.40. \end{aligned} \tag{17}$$

These expectations arise from the MC yields, as follows.

In SRHeavy we find seven $\tau\tau$ events, and nothing else. One of these events contains the decays

$$\tau^+ \to \mu^+ \bar{\nu}_\tau \nu_\mu \ , \quad \tau^- \to \nu_\tau \pi^- K^+ K^-. \tag{18}$$

Both the π^- and the K^+ undergo decay in flight to muons, and the two muons form the DV. The second event contains

$$\tau^+ \to \mu^+ \bar{\nu}_\tau \nu_\mu \ , \quad \tau^- \to \nu_\tau \pi^- K_S. \tag{19}$$

Both pion daughters of the K_S undergo decay to muons, and the two muons form the DV. In SRLight we find 2 $\tau\tau$ events and 2 $q\bar{q}$ events. The $\tau\tau$ events have the decays

$$\begin{aligned} &\tau^+ \to \bar{\nu}_\tau K_L \pi^+ \ , \ \tau^- \to e^- \bar{\nu}_e \nu_\tau, \\ &\tau^+ \to \bar{\nu}_\tau \pi^+ K_L \ , \ \tau^- \to \nu_\tau \rho^-. \end{aligned} \tag{20}$$

In both events the K_L decays to $\mu^\pm \pi^\mp \nu_\mu$, and the pion and muon form the DV.

The first $\bar{q}q$ event is a $s\bar{s}$ event with the final state $K_L, K_S, \pi^+\pi^-\pi^0$. The DV is formed from a pion produced in the K_S decay and from a muon produced in a pion decay.

The second $\bar{q}q$ event is a $u\bar{u}$ event with the final state $K_L, K^-, \pi^+\pi^0$. The DV is formed from two muons, one produced in the K_L decay and the other produced in a pion decay.

Sample	ee	$\mu\mu$	$\tau\tau$	4ℓ	$ee\bar{q}q$	$q\bar{q}$	$B\bar{B}$	MC	σMC	Sig300	Sig1000	Sig1600
Online	1	341	29554	431	194	6793	866	7665	40	69546	73171	72619
$\boldsymbol{N_{\mathrm{tracks}}}$	1	42	20202	101	122	1524	75	4433	30	64803	66760	61105
$\boldsymbol{DL > 15cm}$	0	17	4884	31	33	531	24	1108	15	28959	32125	25448
$\boldsymbol{\chi^2_{prob} > 10^{-5}}$	0	12	2425	8	9	186	5	530	10	27550	28795	22359
$\boldsymbol{cos\theta_{\mu^+\mu^-}}$	0	12	2118	7	8	158	1	462	10	27171	28378	22124
$\boldsymbol{L_{ID}}$ **prompt** $\boldsymbol{\pi}$	0	0	1817	6	2	135	1	392	9	24864	25560	20551
CDC Hits min	0	0	1483	4	0	97	1	317	8	21673	24359	18178
$\boldsymbol{\mu_{ID}}$ **(N) cut 1**	0	0	1208	3	0	81	0	258	7	21575	24258	18117
$\boldsymbol{K^0_S}$ **exclusion**	0	0	116	0	0	13	0	25.8	2.3	21575	21050	17252
$\boldsymbol{\sum E_\gamma}$	0	0	110	0	0	10	0	24.0	2.2	20282	19860	16409
$\boldsymbol{E_{\pi^0}}$	0	0	91	0	0	8	0	19.8	2.0	20038	19622	16240
$\boldsymbol{A_{\mathrm{sq}}}$	0	0	27	0	0	4	0	6.2	1.1	20037	19548	16028
$\boldsymbol{\mu_{ID}}$ **(N) cut 2**	0	0	13	0	0	2	0	3.00	0.77	17695	17239	14455
$\boldsymbol{m^{DV}_{\pi\pi} > 0.52GeV}$	0	0	2	0	0	0	0	0.40	0.28	0	15234	13948
$\boldsymbol{m^{DV}_{\pi\pi} < 0.42GeV}$	0	0	11	0	0	2	0	2.60	0.72	17695	2005	507
$\boldsymbol{m_+, m_-}$	0	0	2	0	0	2	0	0.80	0.40	17681	251	0

TABLE VI: Cut flow table for the SRHeavy and SRLight signal regions, showing the event yield at each stage of the selection for the generic MC samples and selected signal samples with the HNL mass indicat. MC is the total number of events expected in the data sample given the MC yields, and σMC is its uncertainty, arising from MC statistics only.

Fig. 15 shows the distributions of m_- vs. m_+, E_- vs. E_+, and A_{sq} for $\tau^+\tau^-$ background MC events in the SRs (after the final cuts). While the variables E_- and E_+ are not used in our selection, we show them here since they are suggested in Ref. [33]. In practice, after the other cuts, cutting on them is not worthwhile.

Fig. 16 shows the same variables for the $q\bar{q}$ background. Figs. 17, 18, and 19 show these distributions for the 300 MeV, 1000 MeV, and 1600 MeV signal samples. Based on these distributions, we chose to apply the cuts on A_{sq} and on $m_\pm$ but not on $E_\pm$.

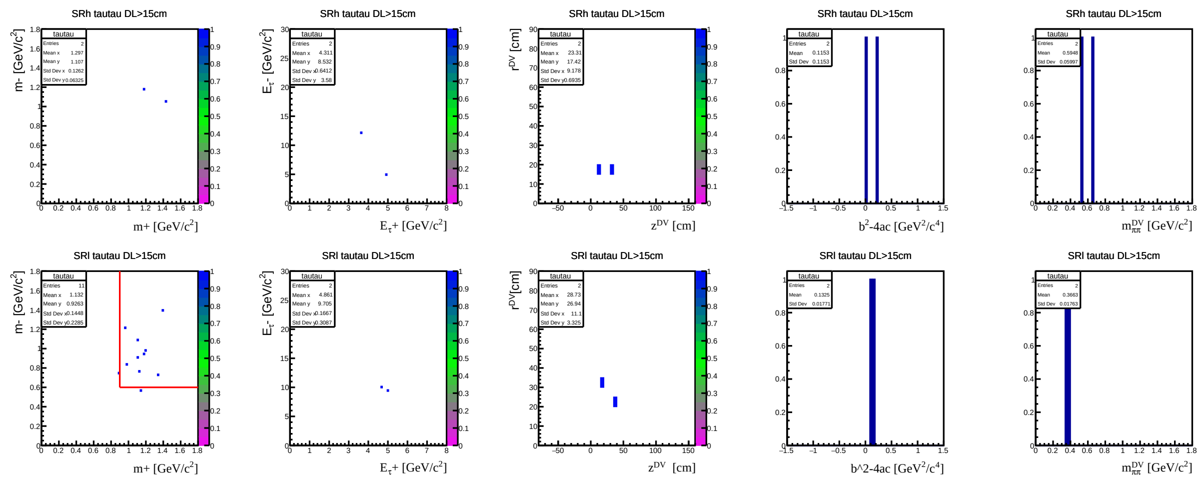

FIG. 15: Distributions of m_- vs. m_+, $E_{\tau-}$ vs. $E_{\tau+}$, $A_{\rm sq}$, r_{DV} vs. z_{DV} and $m_{\pi\pi}^{DV}$ for $\tau^+\tau^-$ background MC events in (top plots) SRHeavy and (bottom plots) SRLight. The red square on the m_- vs. m_+ plot shows the cut that either $m_+ < 0.9$ GeV or $m_- < 0.6$ GeV. This takes advantage of the fact that background events that satisfy $m_{\pi\pi}^{DV} < 0.42$ GeV tend to have high values of $m_\pm$, in contrast with signal.

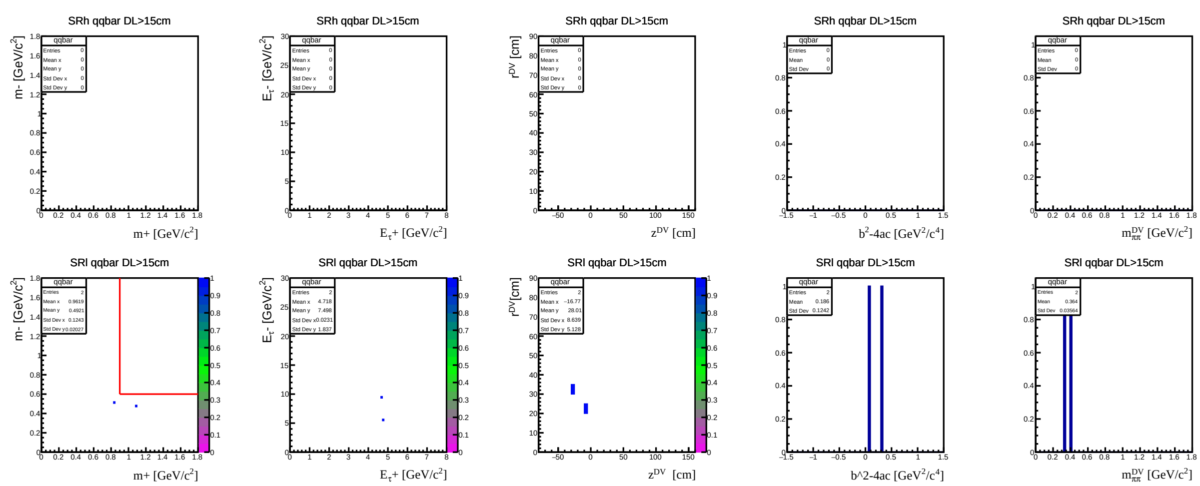

FIG. 16: Same as Fig. 15 for the $q\bar{q}$ background MC.

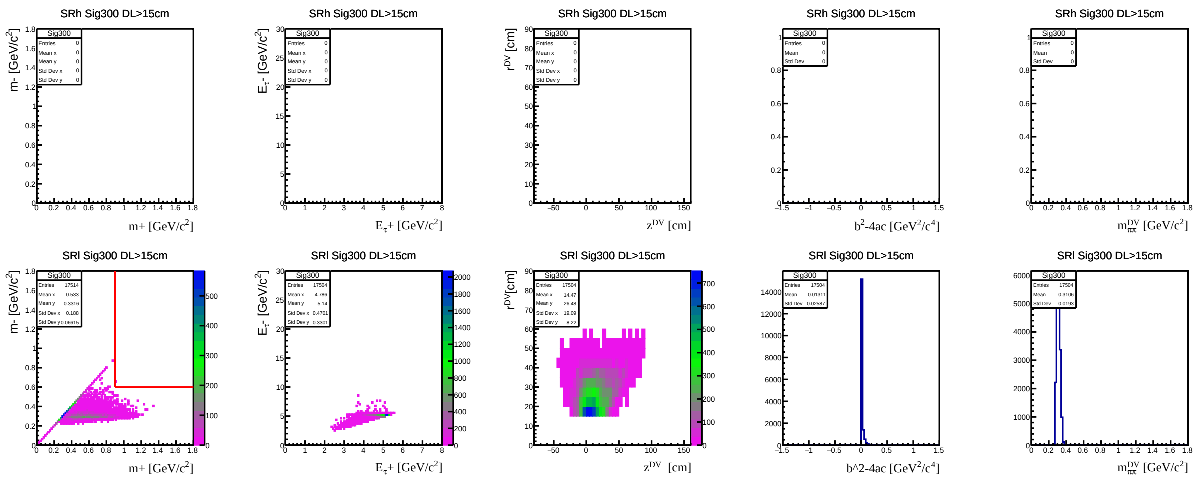

FIG. 17: Same as Fig. 15 for the $m_N = 300$ MeV signal MC events.

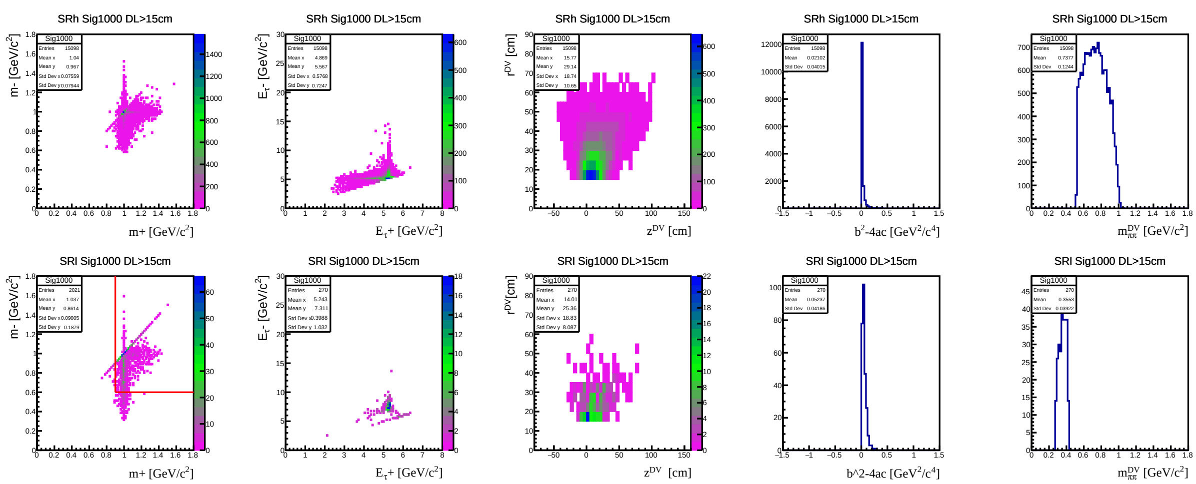

FIG. 18: Same as Fig. 15 for the $m_N = 1000$ MeV signal MC events.

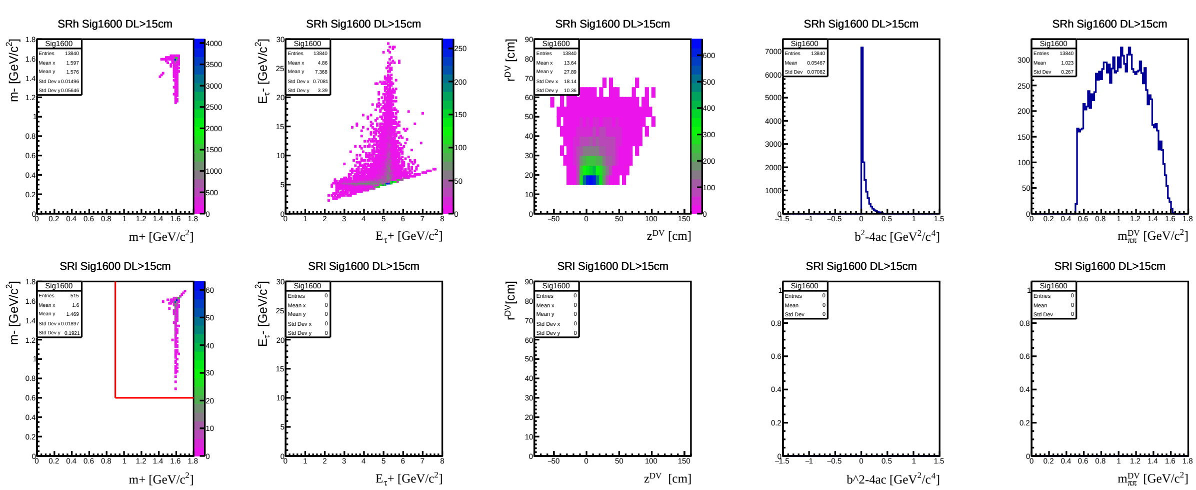

FIG. 19: Same as Fig. 15 for the $m_N = 1600$ MeV signal MC events.

6.3. Control region selection

Two control regions (CRs) are used to estimate the background in the fit described in Sec 10. The two control regions, CRHeavy and CRLight are defined identically to the signal regions SRHeavy and SRLight except that one of the DV tracks is required to be inconsistent with a lepton. This is enforced with the requirement:

- one of the DV daughter tracks satisfies MuonID < 0.01 && ElectronID < 0.01

Table VII compares the cut flow for data and generic MC events where the DV daughters are a pion and a muon, culminating in the two CRs. The table gives the expected (luminosity-scaled MC) and observed (data) CR yields

$$\begin{aligned} N^{MC}_{CRHeavy} &= 73.6 \pm 3.8, \\ N^{data}_{CRHeavy} &= 95 \pm 10, \\ N^{MC}_{CRLight} &= 37.2 \pm 2.7, \\ N^{data}_{CRLight} &= 43 \pm 7. \end{aligned} \tag{21}$$

The table shows that the $N_{\rm data}/N_{\rm MC}$ ratio in CRHeavy is 1.29, and the statistical consistency of this ratio with unity is $(N_{\rm data} - N_{\rm MC})/\sigma = 2.0$, where σ is the total statistical uncertainty on $N_{\rm data} - N_{\rm MC}$. For CRLight this ratio is 1.16, and the consistency is 0.8σ.

We note that the $\tau\tau$ events involve decays that are well understood, including those of the well known, long-lived K_L and K_S. Therefore, we expect the MC to provide a robust prediction of the $\tau\tau$ event yields. The same is not necessarily true of the $q\bar{q}$ simulation, since PYTHIA is rarely tested with low-multiplicity events at this energy scale. Therefore, discrepancy between data and MC is no surprise. However, we can compare the MC events produced in the SRs to those in the CRs, and thus determine whether data-MC comparison in the CR can be used to give a reasonable estimate of the background in the SR. This comparison is carried out in what follows.

In the MC, CRHeavy contains 761 $\tau\tau$ events and 26 $q\bar{q}$ events. The daughters of the DV in the $\tau\tau$ events originate from the following processes:

- 312 events (41%): $K_S \to \pi^+\pi^-$ decays. This includes 70 events (9%) in which the the DV is formed from only one of the K_S daughters.
- 193 events: prompt kaons or pions
- 183 events: decay in flight of prompt kaons or pions
- 62 events: $K_S \to \pi^+\pi^-$ with pion decay in flight
- 11 events: K_L decays

The CRLight contains 101 $\tau\tau$ events and 81 $q\bar{q}$ events, consistent with the two $\tau\tau$ and two $q\bar{q}$ events in SRLight . Among the 101 $\tau\tau$ events, the DV is formed from the following processes:

- 54 events: $K_L \to \pi\mu\bar{\nu}_\mu$
- 26 events: photon conversion
- 15 events: prompt particles
- 4 events: $K_L \to \pi e\bar{\nu}_e$ and $K_L \to \pi\pi\pi^0$
- 2 events: $K_S \to \pi^+\pi^-$ with one decay in flight

Among the 81 $q\bar{q}$ events, the DV arises from the following processes:

- 48 events: $\Lambda \to p\pi$, with 6 events involving pion decay in flight
- 32 events: $K_L \to \pi\mu\bar{\nu}_\mu$
- 1 event: $K_S \to \pi^+\pi^-$

We see that in each CR, the processes that give rise to the DV are statistically consistent with those in the SR. This validates the use of the CRs for estimating the background level in the SRs.

cut	ee	$\mu\mu$	$\tau\tau$	4ℓ	$ee\bar{q}q$	$q\bar{q}$	$B\bar{B}$	MC	σMC	**data**	σ**Data**	$\frac{data}{MC}$	**cons.**
Online	22	15071	2097913	66660	18925	462799	51032	545074	333	403387	635	0.74	-198
$\boldsymbol{N_{\mathrm{tracks}}}$	18	4649	1138959	13690	7231	85891	3373	251780	226	199944	447	0.79	-103
$\boldsymbol{DL > 15cm}$	2	856	316299	4934	3039	31557	1333	72015	121	58574	242	0.81	-50
$\boldsymbol{\chi^2_{prob} > 10^{-5}}$	2	259	137726	984	441	9246	193	29835	78	23059	152	0.77	-40
$\boldsymbol{L_{ID}}$ **prompt** $\boldsymbol{\pi}$	2	37	121715	877	252	8170	143	26279	73	20637	144	0.79	-35
$\boldsymbol{\mu\pi_{ID}}$ **(N) cut 1**	0	19	63926	496	178	4471	95	13861	53	11771	108	0.85	-17
$\boldsymbol{\sum E_\gamma}$	0	15	59646	466	165	3808	89	12860	51	10921	105	0.85	-17
$\boldsymbol{E_{\pi^0}}$	0	15	49865	366	164	2498	50	10613	46	9269	96	0.87	-13
$\boldsymbol{cos\theta_{\mu\pi}}$	0	5	41619	247	71	1920	16	8785	42	7649	87	0.87	-12
CDC Hits min	0	0	33688	123	0	1418	5	7047	38	5941	77	0.84	-13
$\boldsymbol{K^0_S}$ **exclusion**	0	0	2993	25	0	278	1	659	11	670	26	1.02	0.39
$\boldsymbol{A_{\mathrm{sq}}}$	0	0	1267	10	0	172	1	290	8	290	17	1.00	0
$\boldsymbol{m^{DV}_{\pi\pi} > 0.52GeV}$	0	0	337	5	0	26	0	73.6	3.8	95	10	1.29	2.00
$\boldsymbol{m^{DV}_{\pi\pi} < 0.42GeV}$	0	0	930	5	0	146	1	216	6	195	14	0.90	-1.4
$\boldsymbol{m_+, m_-}$	0	0	101	3	0	81	1	37.2	2.7	43	7	1.16	0.77

TABLE VII: Cut flow for the control regions CRHeavy and CRLight in data and generic MC. MC and σMC are the total luminosity-weighted MC yield and its MC-statistical uncertainty. data and σData are the data yield and its statistical uncertainty. $\frac{data}{MC}$ is the ratio between the data and total-MC yields, and cons. is the statistical consistency, the difference between the data and luminosity-scaled MC divided by the total statistical uncertainty. See Table VI caption for additional details

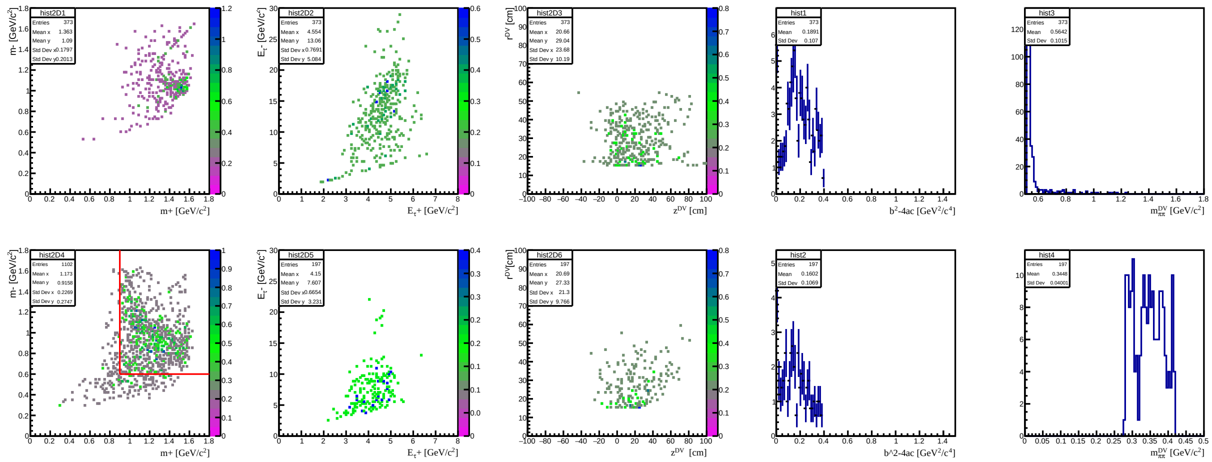

FIG. 20: Distributions of m_- vs. m_+, $E_{\tau-}$ vs. $E_{\tau+}$, r_{DV} vs. z_{DV}, $A_{\rm sq}$ and $m_{\pi\pi}^{DV}$ for $\tau^+\tau^-$ background MC events in (top plots) CRHeavy and (bottom plots) CRLight.

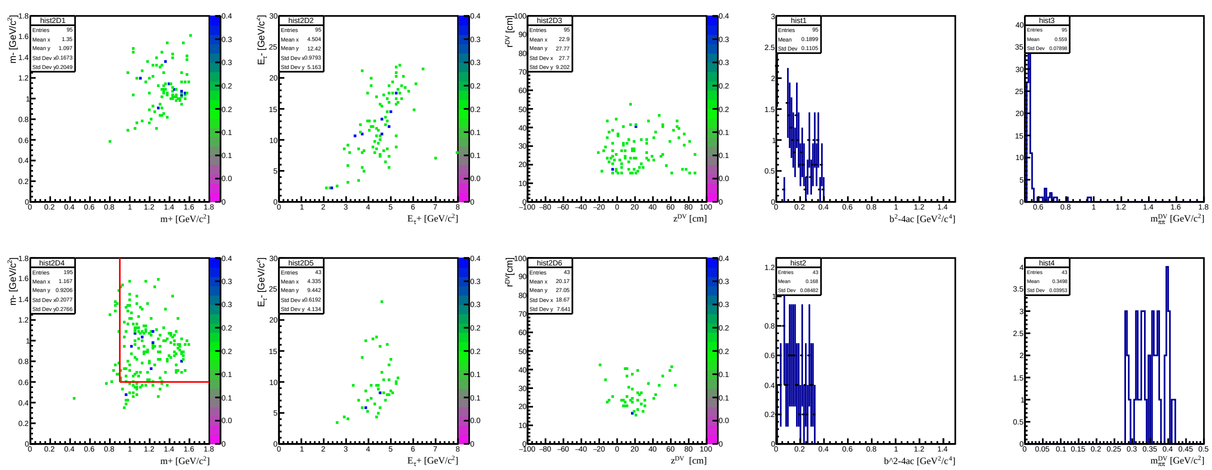

FIG. 21: Same as Fig. 20 for the background data in the CR.

6.4. Validation region selection

MC-data agreement is further tested in the following validation regions (VRs), which are not used in the final fit. The VRs come in pairs, depending on whether they satisfy the $m_{\pi\pi}^{DV}$ and $m_\pm$ cuts that correspond to SRHeavy or SRLight. For each VR, we list below the event selection and show the cut-flow table comparing MC and data. We also compare the data and MC distributions of several key variables.

6.4.1. VRHeavySameSign *and* VRLightSameSign

The events for this validation region are selected in the same way as SR events, except that

- The two muons emanating from the DV have the same electrical charge.

This targets random combinations of tracks that accidentally form a DV regardless of their charges. Due to the low multiplicity, the yields in the same-sign validation regions are expected to be somewhat smaller than those in the SRs. No same-sign events are observed in the the data. In MC, we see one $\tau\tau$ event and one $q\bar{q}$ event in VRHeavySameSign(corresponding to an expectation of 2/5 event in the data). The data and MC cut flows for these regions are shown in Table VIII. Plots of data and MC same-sign events are shown in Fig. 22.

cut	ee	$\mu\mu$	$\tau\tau$	4ℓ	$ee\bar{q}q$	$q\bar{q}$	$B\bar{B}$	MC	σMC	**data**	σ**Data**	$\frac{data}{MC}$	**cons.**
Online	4	3678	99920	1831	2250	9916	757	23983	71	18682	137	0.78	-34
$\boldsymbol{N_{\mathbf{tracks}}}$	3	825	39285	580	1646	1287	61	8966	44	8343	91	0.93	-6
$\boldsymbol{DL > 15cm}$	0	345	15843	488	1342	747	23	3937	29	4199	65	1.07	3.7
$\boldsymbol{\chi^2_{prob} > 10^{-5}}$	0	104	3368	146	595	154	6	954	15	1116	33	1.17	4.5
$\boldsymbol{cos\theta_{\mu\mu}}$	0	52	1725	44	157	64	3	430	10	460	21	1.07	1.3
$\boldsymbol{L_{ID}}$ **prompt** $\boldsymbol{\pi}$	0	5	1544	39	36	53	2	341	8	348	19	1.02	0.3
CDC Hits min	0	1	12	1	0	1	0.8	3.0	0.80	1	1	0.33	-1.6
$\boldsymbol{\mu_{ID}}$ **(N) cut 1**	0	1	11	1	0	1	0	2.8	0.77	1	1	0.36	-1.4
$\boldsymbol{K^0_S}$ **exclusion**	0	1	11	1	0	1	0	2.8	0.77	1	1	0.36	-1.4
$\boldsymbol{\sum E_\gamma}$	0	1	11	1	0	1	0	2.8	0.77	1	1	0.36	-1.4
$\boldsymbol{E_{\pi^0}}$	0	1	8	1	0	1	0	2.2	0.69	0	0	0	-3.2
$\boldsymbol{A_{\mathbf{sq}}}$	0	1	7	1	0	1	0	2.0	0.66	0	0	0	-3.0
$\boldsymbol{\mu_{ID}}$ **(N) cut 2**	0	1	1	1	0	1	0	0.80	0.45	0	0	0	-1.8
$\boldsymbol{m^{DV}_{\pi\pi} > 0.52GeV}$	0	0	0	0	0	0	0	0	0	0	0	0/0	0/0
$\boldsymbol{m^{DV}_{\pi\pi} < 0.42GeV}$	0	1	1	1	0	1	0	0.80	0.45	0	0	0	-1.8
$\boldsymbol{m_+,m_-}$	0	0	1	0	0	1	0	0.40	0.28	0	0	0	-1.3

TABLE VIII: Data and MC cut flows for the VRHeavySameSign and VRLightSameSign validation regions. See the Table VII caption for additional details

6.4.2. VRHeavy$\pi\pi$ *and* VRLight$\pi\pi$

The events for this validation region are selected in the same way as SR events, except that both DV daughters are inconsistent with being leptons. This is enforced with the requirement

- both DV daughters satisfy MuonID < 0.01 && ElectronID < 0.01

Containing 2 pions instead of 2 muons, these validation regions are "twice removed" from the SRs in that they contain two pions instead of two leptons, so they are less interesting than the control regions. However, they can be taken as a measure of the quality of the simulation of the K_S mass tails and of random dipion combinations.

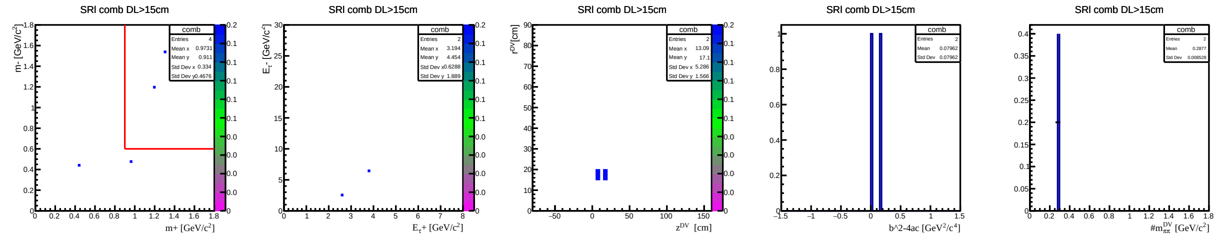

FIG. 22: Distributions of m_- vs. m_+, $E_{\tau-}$ vs. $E_{\tau+}$, r_{DV} vs. z_{DV}, $A_{\rm sq}$ and $m^{DV}_{\pi\pi}$ for $\tau^+\tau^-$ background MC events in (top plots) VRHeavySameSign and (bottom plots) VRLightSameSign.

706 The data and MC cut flows for this VR are shown in Table IX. The data/MC yield ratio
707 is 1.4 in VRHeavy$\pi\pi$and 1.2 in VRLight$\pi\pi$. The consistencies are 4.6 and 1.2, respectively.
708 Thus, the MC somewhat underpredicts the yields in this VR. Plots of MC and data events
709 in these VRs are shown in Figs. 23 and 24.

cut	ee	$\mu\mu$	$\tau\tau$	4ℓ	$ee\bar{q}q$	$q\bar{q}$	$B\bar{B}$	MC	σMC	**data**	σ**Data**	$\frac{data}{MC}$	**cons.**
textbfOnline	70969	24697	5385198	289389	53534	1522327	57573	1701280	1014	1632981	1278	0.96	-42
$\boldsymbol{N_{\rm tracks}}$	48142	13231	2615418	58702	21710	257352	3330	751236	785	774099	880	1.03	19
$\boldsymbol{DL > 15cm}$	5659	3734	595090	20565	14208	89813	1148	164955	297	168794	411	1.02	8
$\boldsymbol{\chi^2_{prob} > 10^{-5}}$	3084	1638	234849	3180	1902	22457	180	62985	206	62358	250	0.99	-1.9
$\boldsymbol{L_{ID}}$ **prompt** $\boldsymbol{\pi}$	889	204	207211	2695	346	19938	110	48998	136	46712	216	0.95	-9
$\boldsymbol{\pi_{ID}}$ **(N) cut 1**	150	20	132620	1834	104	15060	57	30434	87	30409	174	1.00	-0.13
$\boldsymbol{\sum E_\gamma}$	126	10	123374	1742	96	12916	52	28055	83	27987	167	1.00	-0.36
$\boldsymbol{E_{\pi^0}}$	125	10	98905	1344	95	8291	27	22148	75	22754	151	1.03	3.6
$\boldsymbol{cos\theta_{\pi^+\pi^-}}$	123	6	81426	838	34	6563	18	18176	69	18873	137	1.04	5
CDC Hits min	81	1	68673	441	5	5085	14	15104	62	15393	124	1.02	2.1
$\boldsymbol{K^0_S}$ **exclusion**	71	1	3327	90	3	1956	2	1304	31	1613	40	1.24	6
$\boldsymbol{A_{\rm sq}}$	25	1	1393	40	1	1236	0	615	19	856	29	1.39	7
$\boldsymbol{m^{DV}_{\pi\pi} > 0.52GeV}$	0	0	660	13	0	281	0	191	6	273	17	1.43	5
$\boldsymbol{m^{DV}_{\pi\pi} < 0.42GeV}$	25	1	733	27	1	955	0	424	18	583	24	1.38	5
$\boldsymbol{m_+,m_-}$	1	1	182	12	0	423	0	127	6	165	13	1.3	2.7

TABLE IX: Data and MC cut flows for the VRHeavy$\pi\pi$ validation regions. See the Table VII caption for additional details

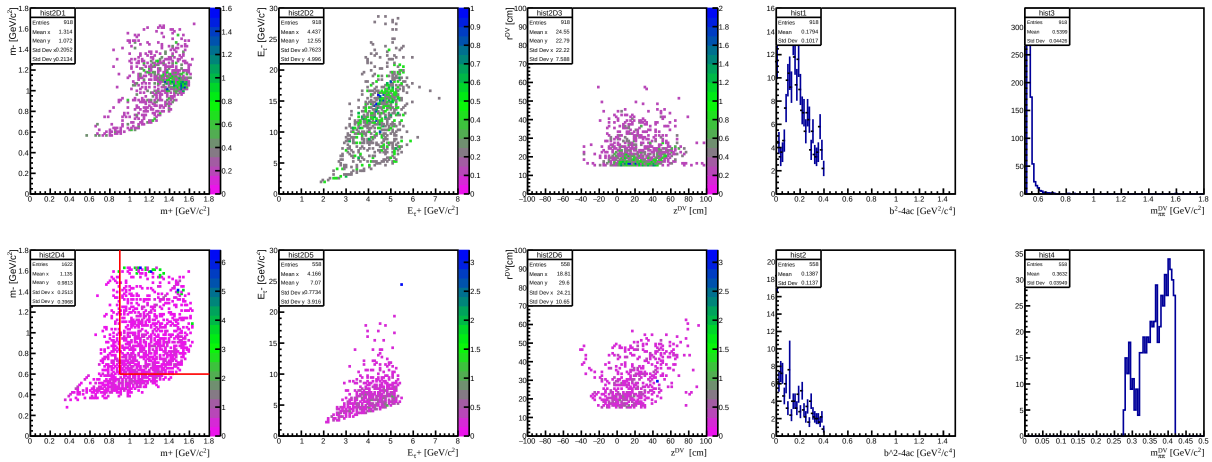

FIG. 23: Distributions of m_- vs. m_+, $E_{\tau-}$ vs. $E_{\tau+}$, r_{DV} vs. z_{DV}, $A_{\rm sq}$ and $m_{\pi\pi}^{DV}$ for $\tau^+\tau^-$ background MC events in (top plots) VRHeavy$\pi\pi$ and (bottom plots) VRLight$\pi\pi$.

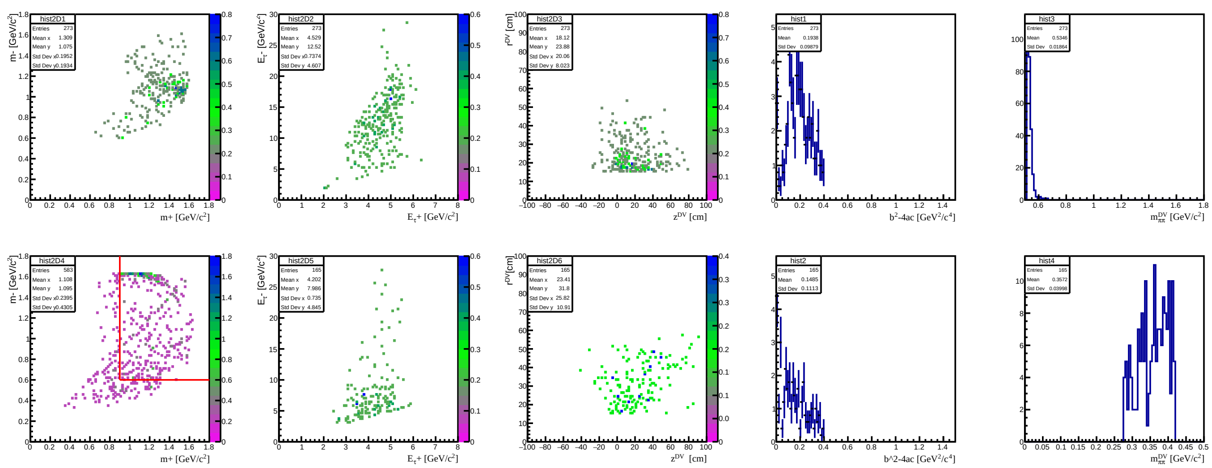

FIG. 24: Same as Fig. 23 for the background data in the pipi validation regions

6.4.3. VRK_S

This validation region selects the decays $\tau^- \to \pi^- K_S \nu$, $K_S \to \pi^+\pi^-$. Candidates are selected in the same way as the signal-region events, except that

- both DV daughters satisfy MuonID < 0.01 && ElectronID < 0.01
- $480 < m_{\pi\pi}^{DV} < 515$ MeV.

The data and MC cut-flow for this region are shown in Table X. The $m_{\pi\pi}^{DV}$ distribution for the selected events is shown in Fig. 25 for different regions of $r_{\rm DV}$. We see that the $m_{\pi\pi}^{DV}$ distribution is more shifted to the right the larger $r_{\rm DV}$ is. We do not understand the source of this effect (perhaps magnetic field calibration or wrong assumption of the amount of material traversed by highly displaced tracks), but in any case it is well simulated in the

MC. We note that these distributions are identical to the "untampered" mass distributions that come out of basf2. Therefore, the shift to the right is not due to the change of track mass hypothesis when calculating $m_{\pi\pi}^{DV}$. in any case, this shift does not affect our analysis.

cut	ee	$\mu\mu$	$\tau\tau$	4ℓ	$ee\bar{q}q$	$q\bar{q}$	$B\bar{B}$	MC	σMC	**data**	σ**Data**	$\frac{data}{MC}$	**cons.**
$\boldsymbol{480 < m_{\pi\pi}^{DV} < 515 GeV}$	1	0	62645	289	0	2197	12	13031	51	12717	112	0.98	-2.5
$\boldsymbol{A_{\mathrm{sq}}}$	1	0	37141	79	0	1403	3	7728	39	7917	88	1.02	1.9
$\boldsymbol{m_+, m_-}$	0	0	569	30	0	391	2	198	6	277	16	1.40	4.4

TABLE X: Data and MC cut flows for the VRK_S validation regions. Here we see only the last cuts of the flow. See Table IX caption for full cut flow up to these cuts, and for additional details.

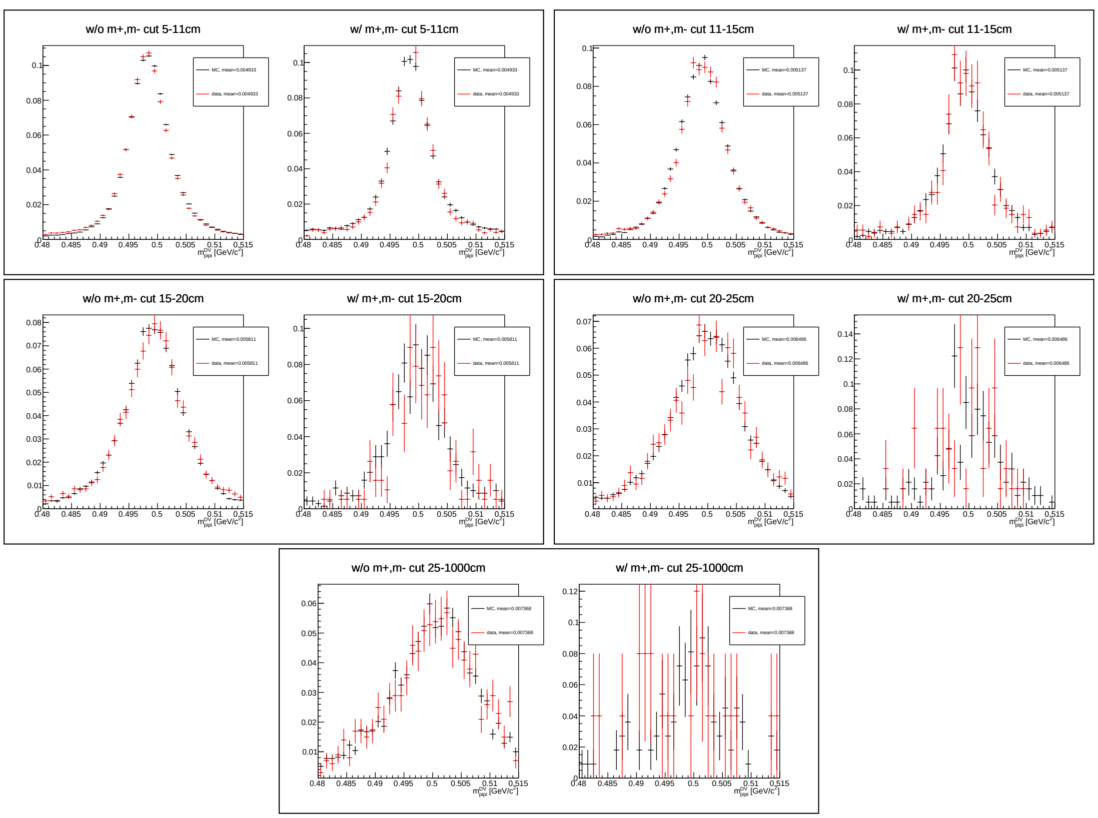

FIG. 25: Comparison of the $m_{\pi\pi}^{DV}$ distribution of MC (black) and data (red) candidates in the VRK_S validation region, for different regions of r_{DV} as indicated on each plot. In each pair of plots, the left (right) plot is without (with) the cut on m_+ and m_- used to define the SRLight and CRLight regions.

7. SIGNAL EFFICIENCY AND EXPECTED NUMBER OF SIGNAL EVENTS

The signal MC is generated with a particular value $c\tau_0$ of the lifetime, so a method for calculating the efficiency for any given lifetime $c\tau_1$ is needed. A simple method is by reweighting, described in Appendix B. A problem with this method is that it fails when τ_1 and τ_0 are very different and MC statistics is finite, as we show in Appendix B.

Therefore, we are using another approach: we use each MC sample to obtain a binned efficiency map in terms of the DV position,

$$\epsilon_b = \frac{P_b}{G_b} \tag{22}$$

where b is the index of the bin centered at the radial and longitudinal DV position $(r_{\rm DV}, z_{\rm DV})$, G_b is the number of signal events generated in this bin, and P_b is the number of these events that passed the selection. These efficiency maps are shown in Fig. 26. Subsequently, for each of the $G = \sum_b G_b$ events in the signal sample we randomly draw R "toy" values of the lifetimes t_r from an exponential distribution $\frac{1}{\tau_1}\exp(-t_r/\tau_1)$. For each value of t_r we calculate a decay position

$$\begin{aligned} r_{\rm DV}^{gr} &= \frac{p_T^g}{m_N} c t_r \\ z_{\rm DV}^{gr} &= \frac{p_z^g}{m_N} c t_r, \end{aligned} \tag{23}$$

where p_T^g, p_z^g, and m_N are the true transverse momentum, longitudinal momentum, and invariant mass of the HNL in signal-MC event g. The total efficiency is then

$$\epsilon = \frac{1}{GR}\sum_{g=1}^{G}\sum_{r=1}^{R}\epsilon_{b(gr)}, \tag{24}$$

where $b(gr)$ is the bin corresponding to position $(r_{\rm DV}^{gr}, z_{\rm DV}^{gr})$ in the efficiency map. This can be rewritten as a sum over the bins,

$$\epsilon = \frac{1}{N}\sum_b N_b \epsilon_b, \tag{25}$$

where N_b is the total number of toy events in bin b, and $N = \sum_b N_b$ is the total number of toy events. From the last expression we obtain the MC-statistical squared uncertainty on the efficiency,

$$\sigma_\epsilon^2 = \frac{1}{N^2}\sum_b \left[N_b^2 \frac{1}{G_b}\epsilon_b(1-\epsilon_b) + N_b \epsilon_b^2\right], \tag{26}$$

where we took the uncertainty on ϵ_b to be binomial.

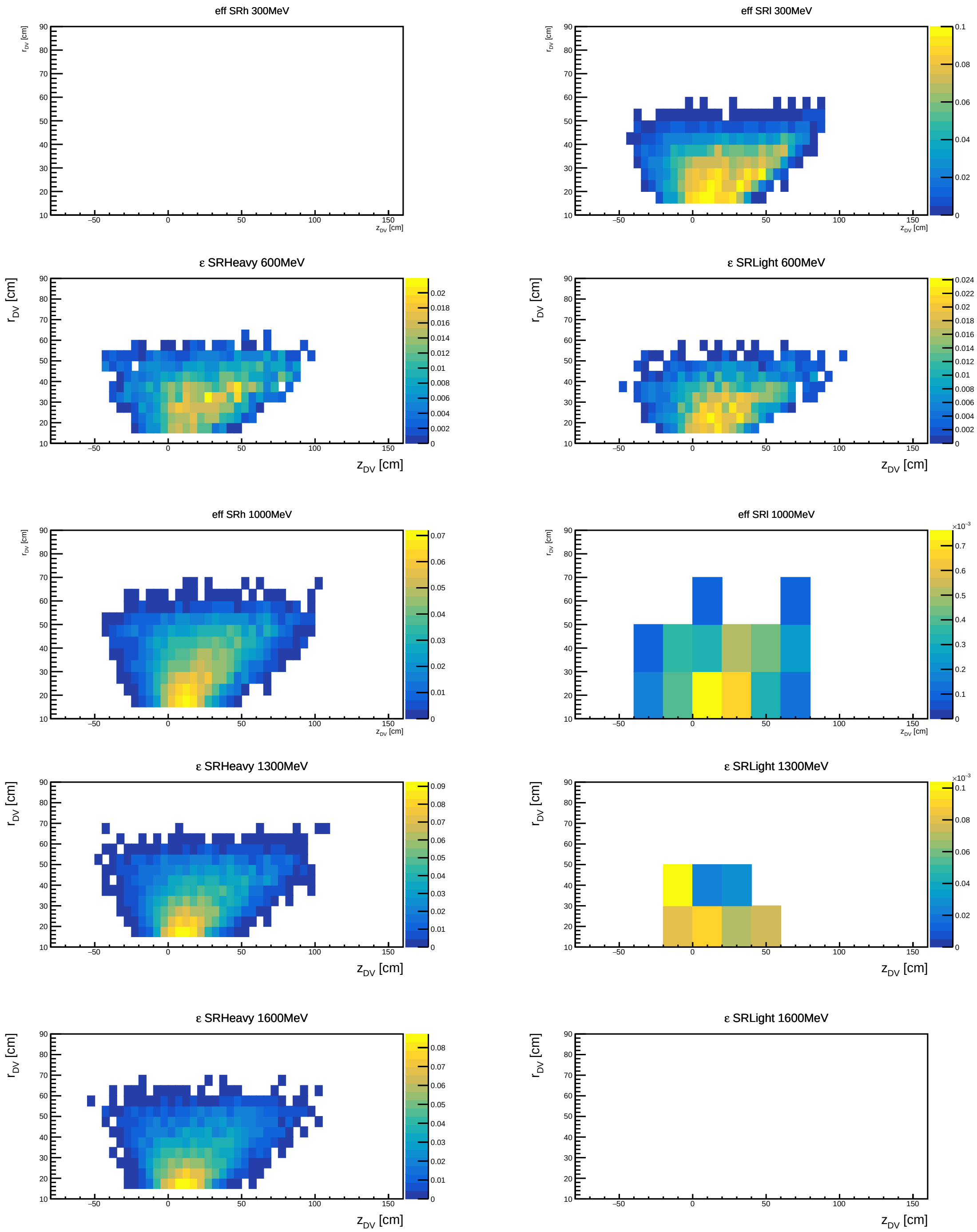

FIG. 26: Efficiency maps, calculated as described in Eq. (22), for SRHeavy (left plots) and SRLight (right plots) of signal samples of 300,600,1000,1300,1600 MeV. White bins have lower entries than the z-axis scale.

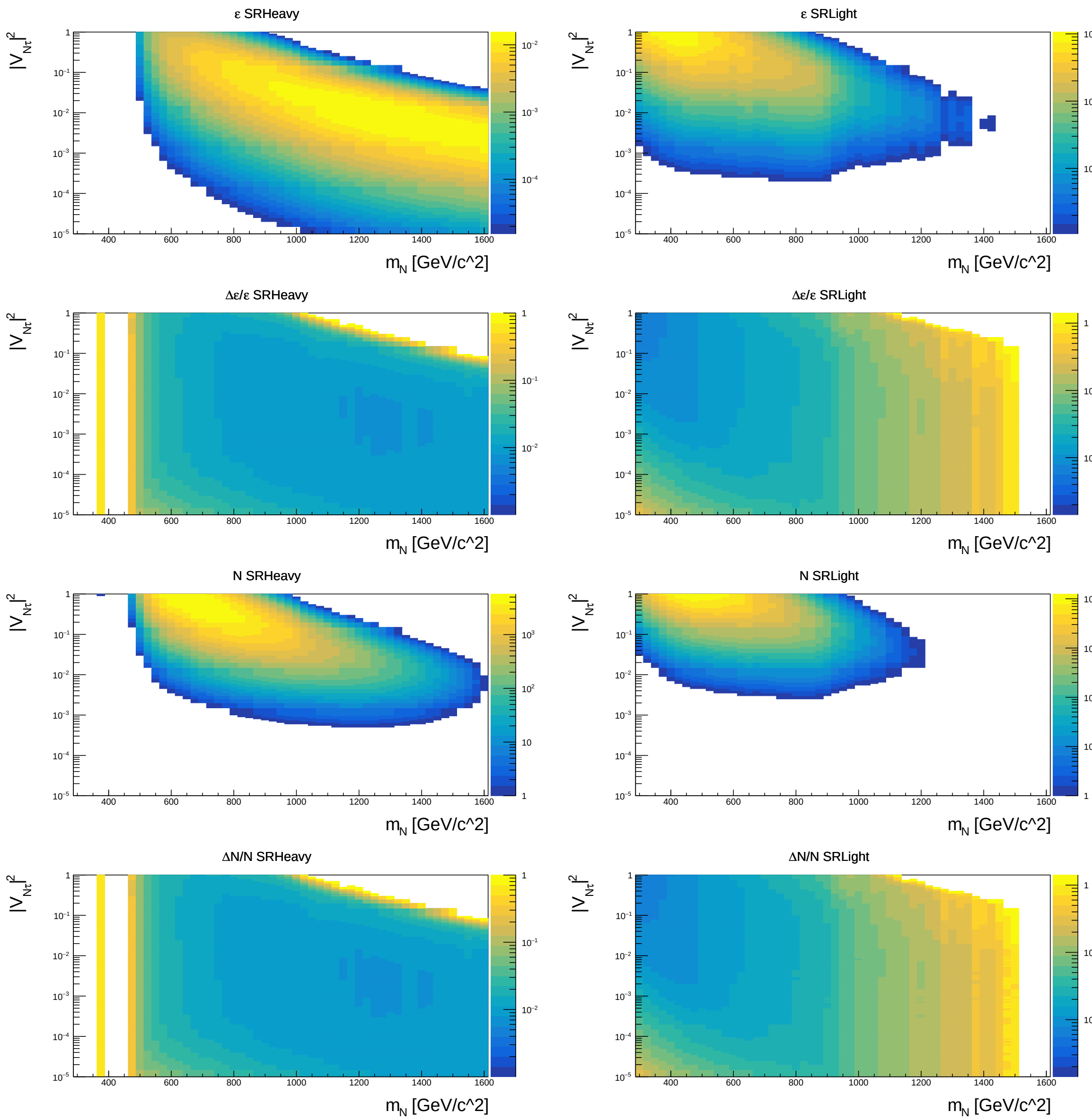

FIG. 27: The total efficiencies (first row), their relative uncertainties (second row), the expected numbers of signal events (third row), and their relative uncertainties (fourth row) as functions of $V_{\tau N}$ and m_N for SRHeavy (left column) and SRLight (right column). White bins have lower entries than the minimal z-axis range shown.

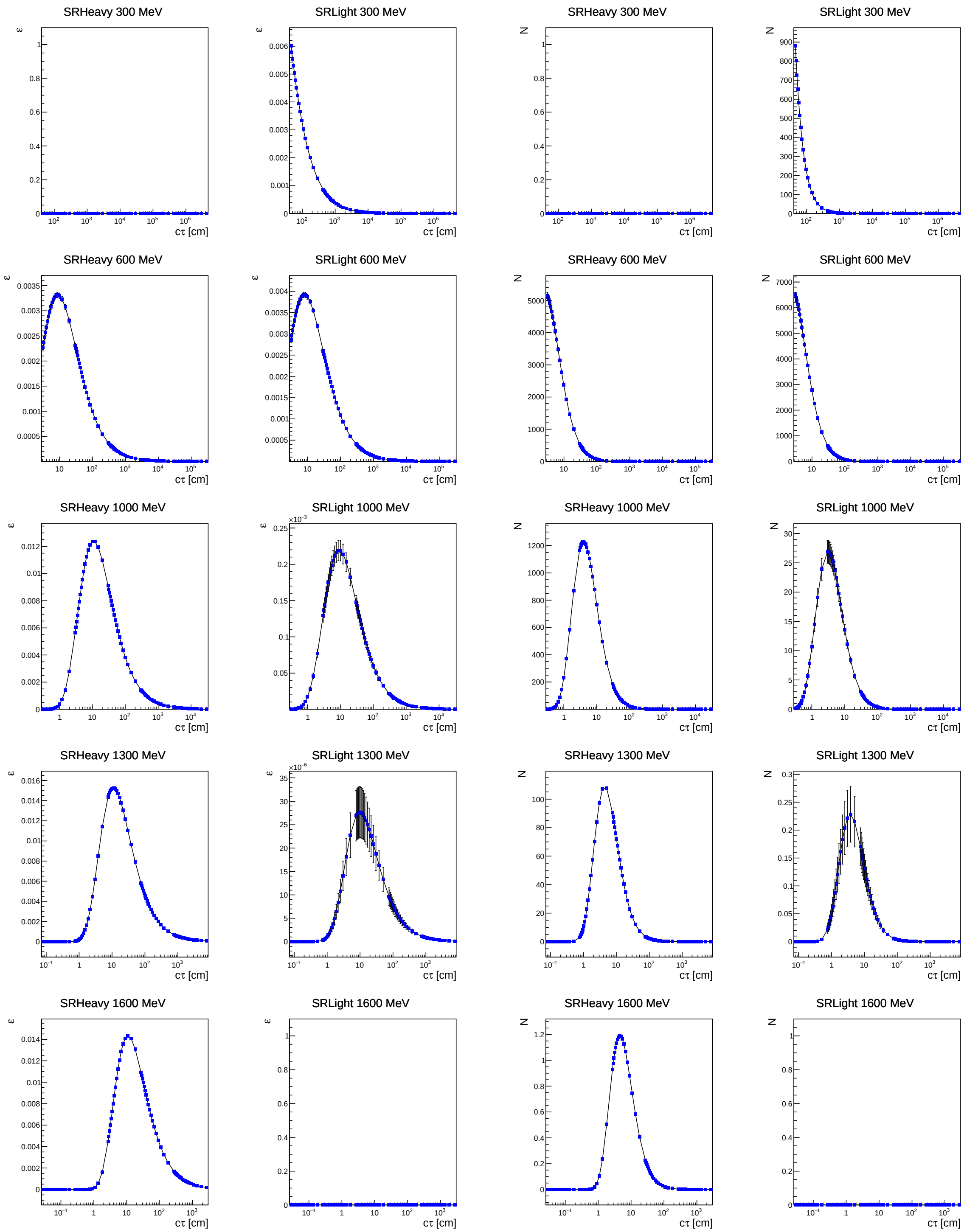

FIG. 28: Efficiency ε and expected number of signal events N as functions of $c\tau_1$ in the SRHeavy and SRLight for the signal samples of $m_N = 300, 600, 1000, 1300, 1600$ MeV

8. SYSTEMATIC UNCERTAINTIES

All systematic uncertainties are treated with Gaussian nuisance parameters applied to the signal or background model in the statistical analysis described in Sec. 10. These uncertainties are as follows:

- Background prediction: we take the relative systematic uncertainty to be the percentage change in the background model needed to bring the data and MC to 1σ agreement in the CRs and the $\pi\pi$ VRs). Specifically,

$$\sigma(N_{\text{bgd}}) = \left(\frac{N_{\text{data}} - N_{\text{MC}}}{\sigma(N_{\text{data}} - N_{\text{MC}})} - 1\right) \frac{\sigma(N_{\text{data}} - N_{\text{MC}})}{N_{\text{MC}}}, \tag{27}$$

  where

$$\sigma(N_{\text{data}} - N_{\text{MC}}) = \sqrt{\sigma^2_{\text{MC}} + N_{\text{data}}} \tag{28}$$

  is the statistical uncertainty on $N_{\text{data}} - N_{\text{MC}}$. If Eq. (27) yields a negative value, the data and MC are consistent to within the available statistics, and we take the uncertainty to be 0. The values of $\sigma(N_{\text{bgd}})$ extracted from the CRs and VRs are shown in Table XI. For the final systematic we use the most conservative value of 34%, taken from VRHeavy$\pi\pi$. This uncertainty is taken to be uncorrelated among the bins (see Sec. 10).

- MC statistical errors, as described in Eq. (26). Uncorrelated among the bins.

- Signal model: our signal MC is generated with a phase-space distribution. To determine the impact of this on the efficiency, we use events with MadGraph. MadGraph is another generator, which consider that proper matrix element for the decay, so the distributions might not be flat [55]. The MadGraph samples generated for us by Nicolas Neil, a co-author of Ref. [33]. The model used in MadGraph is the SM + Majorana neutrinos [56] modified with an effective vertex of the form $\partial_\mu \pi \bar{\tau} \gamma^\mu (1 - \gamma_5) N + h.c$ to generate the $\tau^- \to \pi^- N$ decay.

  Distributions of the MadGraph-generated events are shown in Figs. 29 and 30. In Fig. 29 we see that the distribution for $\cos\theta_d^\tau$ of the decay angle of the τ, defined as the angle between the CM frame and the HNL in the τ rest frame, is flat, as it is in the phase-space model used in our KKMC+PYTHIA events. This is also the case for the distribution for $\cos\theta_d^N$ of the decay angle of the HNL, defined as the angle between

Sample	Uncertainty
CRHeavy	0.15
CRLight	0
VRHeavy$\pi\pi$	0.34
VRLight$\pi\pi$	0.19

TABLE XI: Options for the relative systematic uncertainty on the background yield extracted from different samples according to Eq. (27). The final systematic used is the most conservative value, from VRHeavy$\pi\pi$

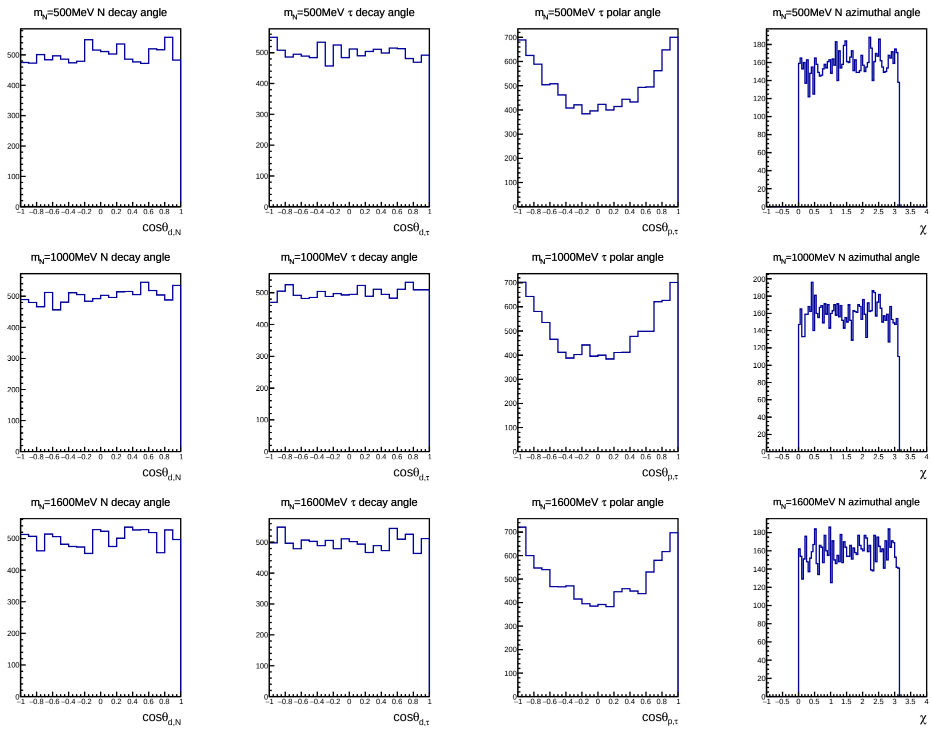

FIG. 29: Distributions of the cosines of the decay angle of the HNL (left column), the decay angle of the τ (2nd column), the polar angle of the τ (3rd column), and the angle between the decay planes (right column) for HNL masses of 500 (top row), 1000 (middle row), and 1600 MeV (bottom row) in events generated with MadGraph.

the τ and the plane of the 3-body HNL decay products in the HNL rest frame. We also show in Fig. 29 the flatly (i.e., phase-space) distributed angle χ between the plain $\vec{p}_\tau \times \vec{p}_\pi$ defined by the τ and pion momenta and the plain $\vec{p}_\tau \times \vec{p}_\nu$ defined by the τ and neutrino momenta, all in the HNL rest frame. The events are flat in χ, as Fig. 29 also shows the distribution of the τ polar angle in the CM frame, demonstrating that it is generated correctly according to a $1 + \cos^2\theta$ distribution.

In contrast to these angles, Fig. 30 shows that while the Dalitz plots of the KKMC events are flat, as expected, this is not the case for the MadGraph events. Specifically, MadGraph generates more low-$m_{\mu^+\mu^-}$ events. As a result, the MadGraph events tend to also have lower values of $m_{\pi\pi}^{DV}$, causing a shift of events from SRHeavy to SRLight.

Therefore, to calculate the systematic uncertainty, we weight our signal events by the ratio between the MadGraph and KKMC Dalitz-plot histograms and recalculate the change in efficiency.

This uncertainty is taken to be uncorrelated among the bins.

It should be mentioned that not all MadGraph files have been generated yet, so at this moment we cannot apply this uncertainty. Instead, a conservative constant uncertainty of 20% was used in the final fit, but it will be changed in the near future.

- Luminosity: 1.4% [57]. Correlated for signal and background and among all regions.

- $\sigma(e^+e^- \to \tau^+\tau^-)$: 0.3% [57]. Correlated for signal and background and among all

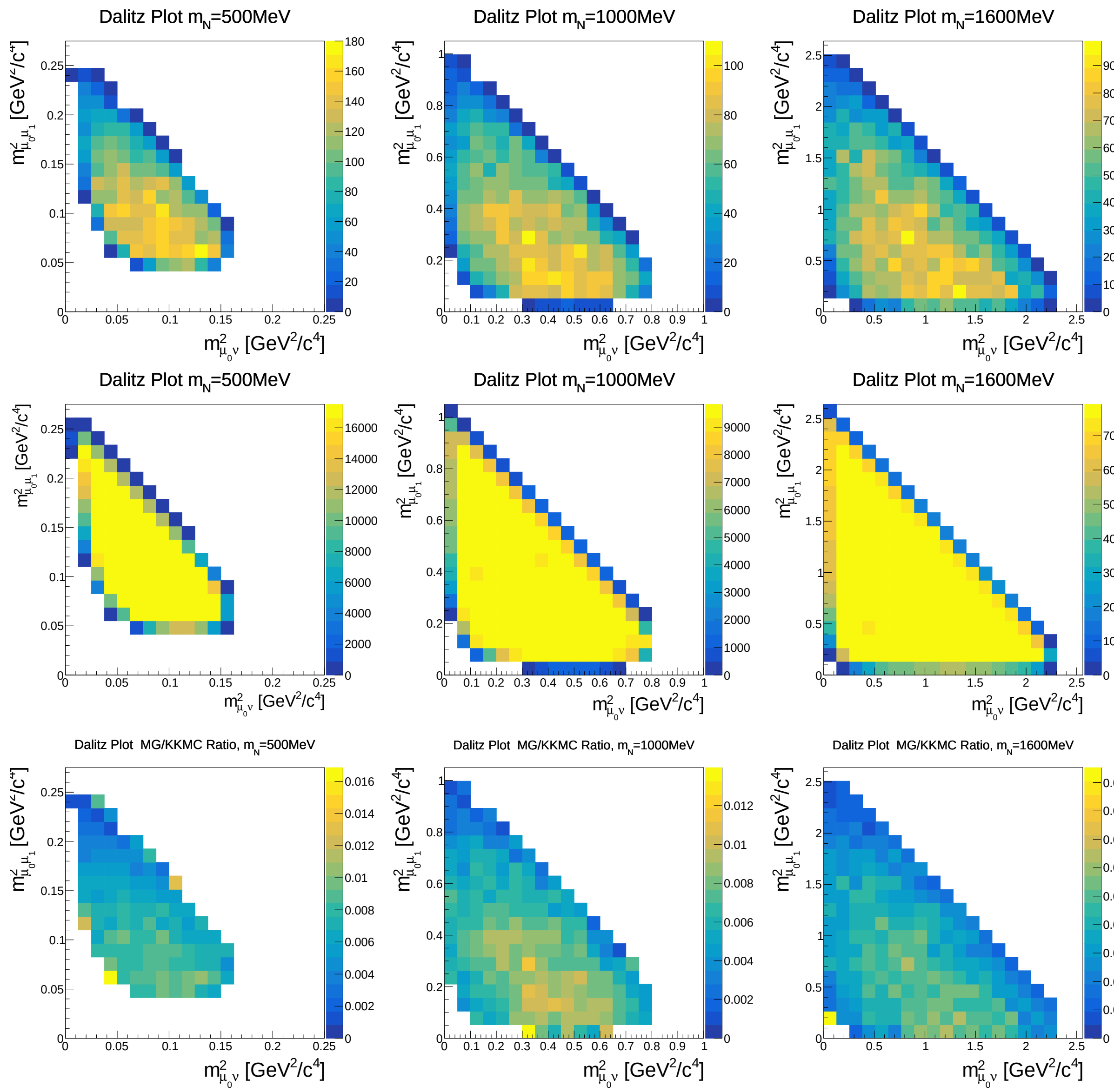

FIG. 30: Dalitz plots for the HNL decay for samples generated with MadGraph (top row) and KKMC (middle row) with $m_N = 500, 1000, 1600$ MeV, and the ratio between the histograms (bottom row), which is used to weight the KKMC-generated events to obtain the signal-model systematic uncertainty.

regions. For the background, it is scaled by the $\tau\tau$ contribution as predicted by the MC.

- $\mathcal{B}(\tau^+ \to 1 - \text{prong})$: $(85.24 \pm 0.06)\%$ (see Table I)

- $\sigma(e^+e^- \to q\bar{q})$: it is anticipated that the continuum MC may not be accurate in the very restricted phase space of our selection, but it is not clear what the relevant systematic uncertainty should be. Therefore, we do not associate a specific value with this uncertainty. Rather, its effect is covered by the uncertainty extracted from the data-MC agreement in the VRs (above).

- Tracking: 0.35% per prompt track [57], totalling 0.7% for the two tracks. Correlated for signal and background and among all regions.

- displaced-track tracking and vertexing: we apply the method of Eq. (27) to the VRK_S, which contains a high-purity sample of K_S decays. The resulting uncertainty is 1.2%.

- Muon identification: 2% [57] for the SRs, 1% for the CRs. Correlated for signal and background and among all regions.

- Trigger: 1.2% [58]. Correlated for signal and background and among all regions.

9. UNBLINDING PLAN

We propose to first unblind the data up to cut #10, where we require that there is no π^0 on the signal side. From the MC (Table VI, the expected number of background events at that point is 19.8 ± 2.0. Therefore, observation of, e.g., 30 events would be consistent with this expectation at the 2.1σ level. Next, we apply cut #11, $A_{\text{sq}} < 0.4$ while also requiring that events fail cut #12 (which is that both muon candidates have muon ID > 0.9). Table VI predicts 3 ± 0.8 background events. This muon ID veto suppresses the signal efficiency is suppressed down to 12.1%, 12.2%, and 10.2% for the 300, 1000, and 1600 MeV samples. While this is evaluated at the generated lifetime, this suppression is not expected to change significantly for other lifetimes, since muID is dominated by the KLM.

Sample	ee	$\mu\mu$	$\tau\tau$	4ℓ	$ee\bar{q}q$	$q\bar{q}$	$B\bar{B}$	MC	σMC	Sig300	Sig1000	Sig1600
NOT $\boldsymbol{\mu_{ID}}$ (N) cut 2	0	0	57	0	0	5	0	12.4	1.57	2433	2403	1656
$\boldsymbol{A_{\text{sq}}}$	0	0	20	0	0	2	0	4.4	0.94	2433	2391	1622
$\boldsymbol{m_{\pi\pi}^{DV} > 0.52GeV}$	0	0	5	0	0	0	0	1	0.45	0	2102	1567
$\boldsymbol{m_{\pi\pi}^{DV} < 0.42GeV}$	0	0	15	0	0	2	0	3.4	0.82	2433	289	55
$\boldsymbol{m_+,m_-}$	0	0	0	0	0	1	0	0.2	0.2	2431	33	0

TABLE XII: Changes in the SR and Table VI (starting from E_{π^0} cut line) for the unblinding plan.

Next, we will unblind the SR but without the muon ID cut on the second muons. This will allow detailed comparison between the data and generic MC before final unblinding. If some inconsistency is seen, we will consider whether any additional validation studies are needed before unblinding the SR.

10. STATISTICAL ANALYSIS AND RESULTS

The expected number of signal events is calculated from the product of the luminosity, cross section, tag-side branching fraction, signal branching fractions, and efficiency:

$$N_{\text{sig}} = 2\,\mathcal{L}\,\sigma(e^+e^- \to \tau^+\tau^-)\,\mathcal{B}(\tau \to 1-\text{prong})\,\mathcal{B}(\tau \to \pi N)\,\mathcal{B}(N \to \mu^+\mu^-\nu)\,\epsilon. \tag{29}$$

We use pyhf (see Section 3.3.3 for more details about this software) to calculate exclusion limits based on this expectation and on the observed numbers of events in the two SRs and two CRs. The signal and background models for the SRs and CRs are obtained from the yiels in MC. The observed yields are taken from the data (before unblinding, we take the observed data yield to be 0 in the two SRs).

We define a grid in the m_N vs. $|V_{N\tau}|^2$ parameter space. In m_N, grid points are separated by 25 MeV. In $|V_{N\tau}|^2$, we use 20 points per decade, separated equidistantly in log scale. For each point in this grid we determine the expected number of signal events in SRHeavy and SRLight using the external inputs given in Appendix C and the signal efficiencies in Fig. 27. The expected signal yields in the two signal regions are used as the signal model for pyhf. The background model is taken from Eq. (17). In addition, pyhf uses the observed yields in CRHeavy and CRLight, with a model obtained from the expected MC yields given in Eq. (21). No scaling of the MC is applied by hand. We use nuisance parameters to include all systematic uncertainties in the fit . We use the general HistFactory template to estimate the probability distribution function.

$$P = \underbrace{\prod_{\text{bin } R} \text{Pois}(n_R|\lambda_R(\eta,\chi))}_{\text{main}} \underbrace{\prod_{\text{constraint } \chi} c_\chi(a_\chi|\chi)}_{\text{auxiliary}} \tag{30}$$

where:

- R is the index for the four regions:
  - SRHeavy
  - SRLight
  - CRHeavy
  - CRLight
- Pois is the Poisson function.
- n_R is the number of events observed in region R.
- $\lambda_R(\eta,\chi)$ is the expected number of events in region R, obtained from a sum over signal and background MC.
- η denotes a scaling factor used internally by pyhf.
- χ denotes all the systematics-related parameters (Sec. 8) and the background expectations.
- $c_\chi(a_\chi|\chi)$ is a constraint term (Gaussian or Poisson) that constrains χ to a known value a_χ to within a given uncertainty.

The main and auxiliary components are labelled in the equation.

We perform hypothesis test with 10000 toy experiments for each of these points in the mesh. We use $\tilde{q}$ test statistics. For each point, we calculate, with the help of pyhf, observed CL_s values, expected CL_s values, and expected CL_s values at $\pm1\sigma$ and $\pm2\sigma$. We then draw

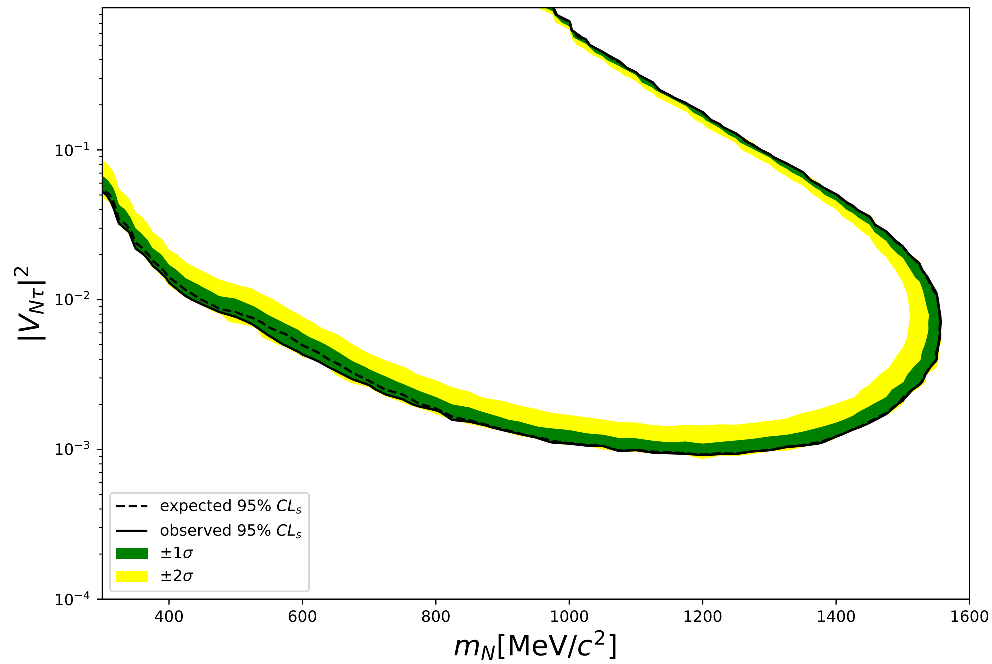

FIG. 31: The expected (dashed) and observed (solid) 95% CL limits on $|V_{N\tau}|^2$ vs. m_N. The green and yellow bands show the 1σ and 2σ bands for the expected limits.

six separate contours which visually represent the 95% CL_s limits. Then we fill between $\pm 2\sigma$ contours with yellow and between $\pm 1\sigma$ contours with green as shown in Fig. 31. It also shows the expected and observed (**before unblinding**, the observed curve assumes 0 events observed in the signal regions) 95% CL limits in the plane of $|V_{N\tau}|^2$ vs. m_N.

This is the main result of the analysis.

11. CONCLUSION

This research sought to discover the HNL, if it exists, with the parameters for which the research is sensitive, and otherwise, to exclude this parameter space. Fig. 31 presents such limits (in $|V_{\tau N}|$ vs. m_N parameter space). Although this thesis does not include the signal data analyses (but only the MC), we can already bring up some points to discuss. By comparing our result to the expectation of Ref. [33] (see Fig. 11), we can notice that the DELPHI result was not significantly improved upon, and for certain, not in the order of magnitude predicted. This is due to the low than expected efficiency we received for our MC samples: The pheno paper's estimates were validated against Belle II MC, but the efficiency at Belle turns out to be significantly smaller. This is particularly the case for muon identification and tracking efficiency of highly displaced tracks. In addition to the efficiency issue, the pheno paper assumed that $\tau \to \pi\pi^0 N$ would be used and also $N \to e^+e^-\nu_\tau$. Since we haven't yet included these, the total sensitivity is lower than expected. Nonetheless, this is the first application of this new method, and with the additional channels and use of Belle II data, the sensitivity is expected to increase to the level predicted in the pheno paper. Of course, the signal model uncertainty that is described in Sec. 8 is still need to be applied and will affect uncertainties bandwidth.

In order to understand this issue better, we work these days on expanding our research, and we additionally analyze the signal side decay chain, where $N \to e^+e^-$. It means that the mass range of interest can go below 300 MeV. Dealing with the e^+e^- channel requires different managing of the selection criteria, which are now studied for the upcoming final decision about them. Hence, results for the e^+e^- channel has yet to be achieved.

As for the unblinding the data of the $\mu^+\mu^-$ channel, we are waiting for the final approval from the recently formed review committee, so we can continue with the plan as described in Sec. 9. If the data and MC are consistent in this region, we will proceed to unblind the SR. If some inconsistency is seen, we will consider whether any additional validation studies are needed before unblinding the SR.

Appendix A: HNL mass calculation

We start with 4-momentum conservation in the τ decay:

$$p_\tau \ = \ p_N + p_x \, . \tag{A1}$$

Solving the above equation gives

$$m_\tau^2 \ = \ m_N^2 + m_x^2 + 2E_N E_x - 2|\vec{p}_N||\vec{q}_x| \ , \tag{A2}$$

where

$$|\vec{q}_x| \equiv |\vec{p}_x| \cos\theta_{Nx} \tag{A3}$$

Similarly, 4-momentum conservation in the HNL (N) decay:

$$p_N \ = \ p_y + p_{\nu_\tau} \ . \tag{A4}$$

Solving the above equation gives

$$0 \ = \ m_N^2 + m_y^2 - 2E_N E_y + 2|\vec{p}_N||\vec{q}_y| \ , \tag{A5}$$

where

$$|\vec{q}_y| \equiv |\vec{p}_y| \cos\theta_{Ny} \tag{A6}$$

Comparing Eqs. (A2) and (A5) gives the solution of HNL energy (E_N) in terms of the magnitude of HNL three momentum ($|\vec{p}_N|$)

$$E_N \ = \ \frac{m_\tau^2 + m_y^2 - m_x^2}{2(E_x + E_y)} + \frac{(|\vec{q}_y| + |\vec{q}_x|)|\vec{p}_N|}{(E_x + E_y)} \tag{A7}$$

$$\Rightarrow E_N \ = \ \mathrm{A} + \mathrm{B}|\vec{p}_N| \tag{A8}$$

where

$$A = \frac{m_\tau^2 + m_y^2 - m_x^2}{2(E_x + E_y)}, \ \ B = \frac{(|\vec{q}_y| + |\vec{q}_x|)}{(E_x + E_y)} \tag{A9}$$

are the two known quantities. 4-momentum relation of HNL is

$$m_N^2 = E_N^2 - |\vec{p}_N|^2 \tag{A10}$$

Expressing the mass of HNL (m_N) in terms of A, B and $|\vec{p}_N|$

$$\Rightarrow m_N^2 = (\mathrm{A} + \mathrm{B}|\vec{p}_N|)^2 - |\vec{p}_N|^2 \tag{A11}$$

Using Eq. (A8) in (A2) gives

$$\Rightarrow m_N^2 \ = \ \frac{(\frac{E_y}{E_x})(m_\tau^2 - m_x^2) - m_y^2}{(1 + \frac{E_y}{E_x})} + \frac{2(\frac{E_y}{E_x}|\vec{q}_x| - |\vec{q}_y|)}{(1 + \frac{E_y}{E_x})}|\vec{p}_N| \tag{A12}$$

$$\Rightarrow m_N^2 \ = \ \mathrm{C} + \mathrm{D}|\vec{p}_N| \tag{A13}$$

where

$$C = \frac{(\frac{E_y}{E_x})(m_\tau^2 - m_x^2) - m_y^2}{(1+\frac{E_y}{E_x})}, \ D = \frac{2(\frac{E_y}{E_x}|\vec{q}_x| - |\vec{q}_y|)}{(1+\frac{E_y}{E_x})} \tag{A14}$$

are the two known quantities.
Comparing Eq. (A11) and Eq. (A13) gives a quadratic equation of the form

$$(\mathrm{B}^2-1)|\vec{p}_N|^2 + (2\mathrm{AB}-\mathrm{D})|\vec{p}_N| + (\mathrm{A}^2-\mathrm{C}) \ = \ 0 \tag{A15}$$

This gives solution of $|\vec{p}_N|$ as

$$|\vec{p}_N| \ = \ \frac{-(2\mathrm{AB}-\mathrm{D}) \pm \sqrt{(2\mathrm{AB}-\mathrm{D})^2 - 4(\mathrm{B}^2-1)(\mathrm{A}^2-\mathrm{C})}}{2(\mathrm{B}^2-1)} \tag{A16}$$

Using Eq. (A16) in Eq. (A13) gives the solution of m_N with 2-fold ambiguity.

Appendix B: The lifetime-reweighting efficiency-calculation method

To calculate the efficiency for a lifetime τ_1 using an MC sample generated with lifetime τ_0, one gives each event a weight

$$w_i = \frac{\tau_0}{\tau_1}\frac{\exp(-t/\tau_1)}{\exp(-t/\tau_0)}, \tag{B1}$$

where t is the true decay time of the HNL in event i. One then obtains the efficiency from the sum of weights:

$$\epsilon = \frac{\sum_p w_p}{\sum_p w_p + \sum_f w_f}, \tag{B2}$$

where the index p runs over the events that passed the cuts, and f runs over all the events that failed the cuts. Writing this as $\epsilon = P/(P+F)$, one can obtain the MC-statistical uncertainty on the efficiency,

$$\sigma_\epsilon^2 = \frac{1}{(P+F)^4}\left[F^2\sum_p w_p^2 + P^2 \sum_f w_f^2\right]. \tag{B3}$$

The problem with this method is that it is biased for large when one has finite MC statistics and τ_1 is very different from τ_0. To see this, we write Eq. (B2) explicitly:

$$\epsilon = \frac{\sum_p \exp(-t_p\alpha))}{\sum_p \exp(-t_p\alpha) + \sum_f \exp(-t_f\alpha)}, \tag{B4}$$

where we define

$$\alpha = \frac{1}{\tau_1} - \frac{1}{\tau_0}. \tag{B5}$$

When statistics is infinite, the sums become integrals, and there is no problem. But for finite samples, we do not have enough statistical precision to differentiate between α and the larger of $1/\tau_0$ or $1/\tau_1$. If we have $\tau_1 \gg \tau_0$, then

$$\alpha \approx -\frac{1}{\tau_0}, \tag{B6}$$

and then

$$\epsilon \approx \frac{\sum_p \exp(t_p/\tau_0))}{\sum_p \exp(t_p/\tau_0) + \sum_f \exp(t_f/\tau_0)}, \tag{B7}$$

which is independent of τ_1. Therefore, at high τ_1, the efficiency becomes τ_1 independent, which is clearly wrong (more events decay outside the detector as τ_1 grows, so the efficiency should drop). In the opposite case, $\tau_1 \ll \tau_0$, we have

$$\epsilon \approx \frac{\sum_p \exp(-t_p/\tau_1))}{\sum_p \exp(-t_p/\tau_1) + \sum_f \exp(-t_f/\tau_1)}, \tag{B8}$$

so the efficiency is independent of how we generated the events (τ_0), which is again obviously wrong.

Appendix C: Cross section, branching fractions, and lifetimes

This appendix shows the model parameters used to calculate the number of signal events produced as a function of M_N and $|V_{\tau N}|^2$.

We use the cross section [38]

$$\sigma(e^+e^- \to \tau^+\tau^-) = 0.919 \pm 0.003 \text{ nb}. \tag{C1}$$

All other parameters are from Ref. [46]. Tables XIII, XIV, and XV show values of $Br(\tau^- \to N\pi^-)$, $Br(N \to \mu^+\mu^-\nu_\tau)$, and the HNL lifetime $c\tau$, respectively. The number of digits is far below the actual uncertainties.

Appendix D: Comparison of efficiency between basf2 vs b2bii for 1 GeV HNL of $c\tau$ = 30 cm

This appendix shows a comparison of efficiency using events generated via KKMC followed by Belle vs Belle II detector simulation

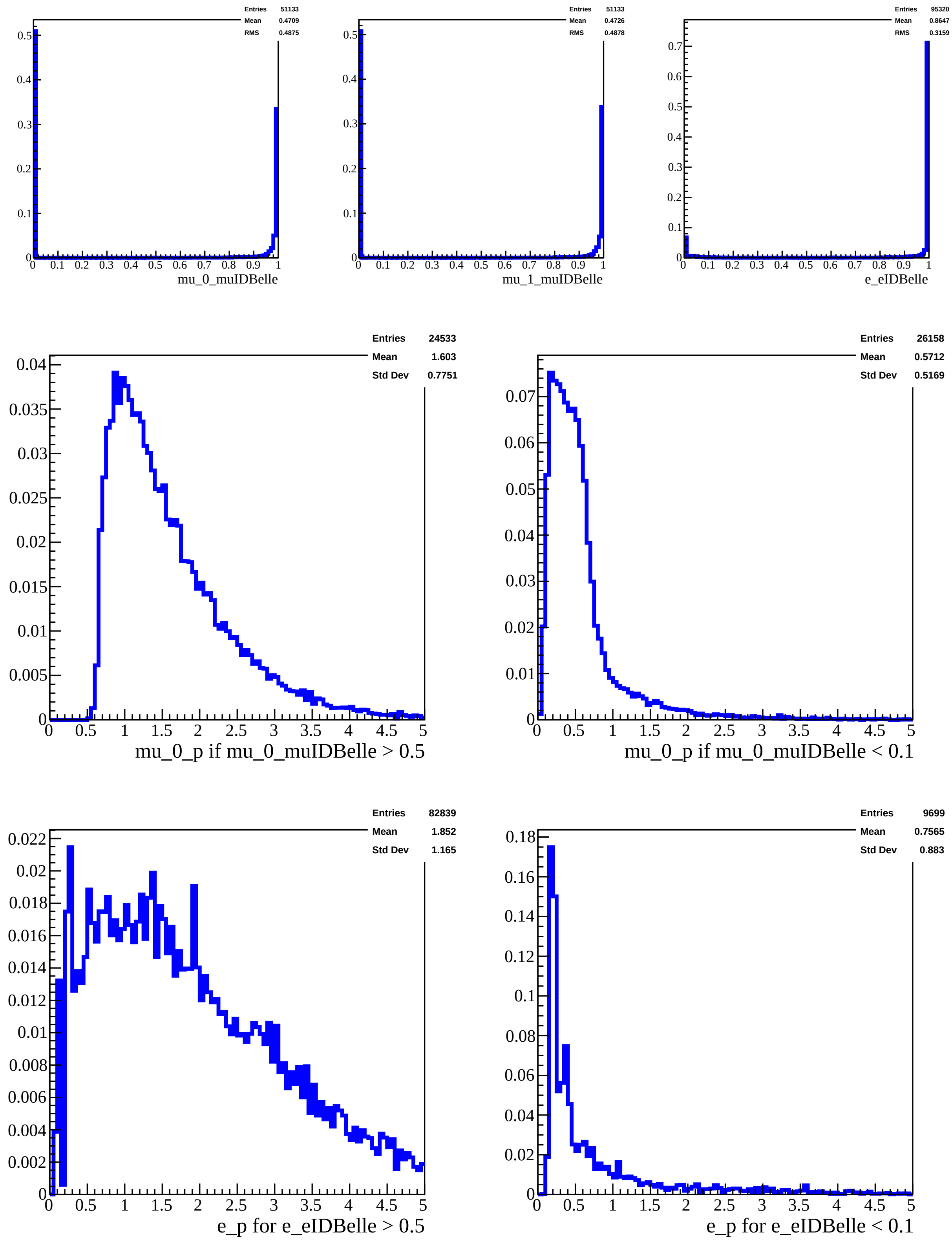

FIG. 32: B2BII lepton ID performances for the signal samples of $m_N = 1000$ MeV

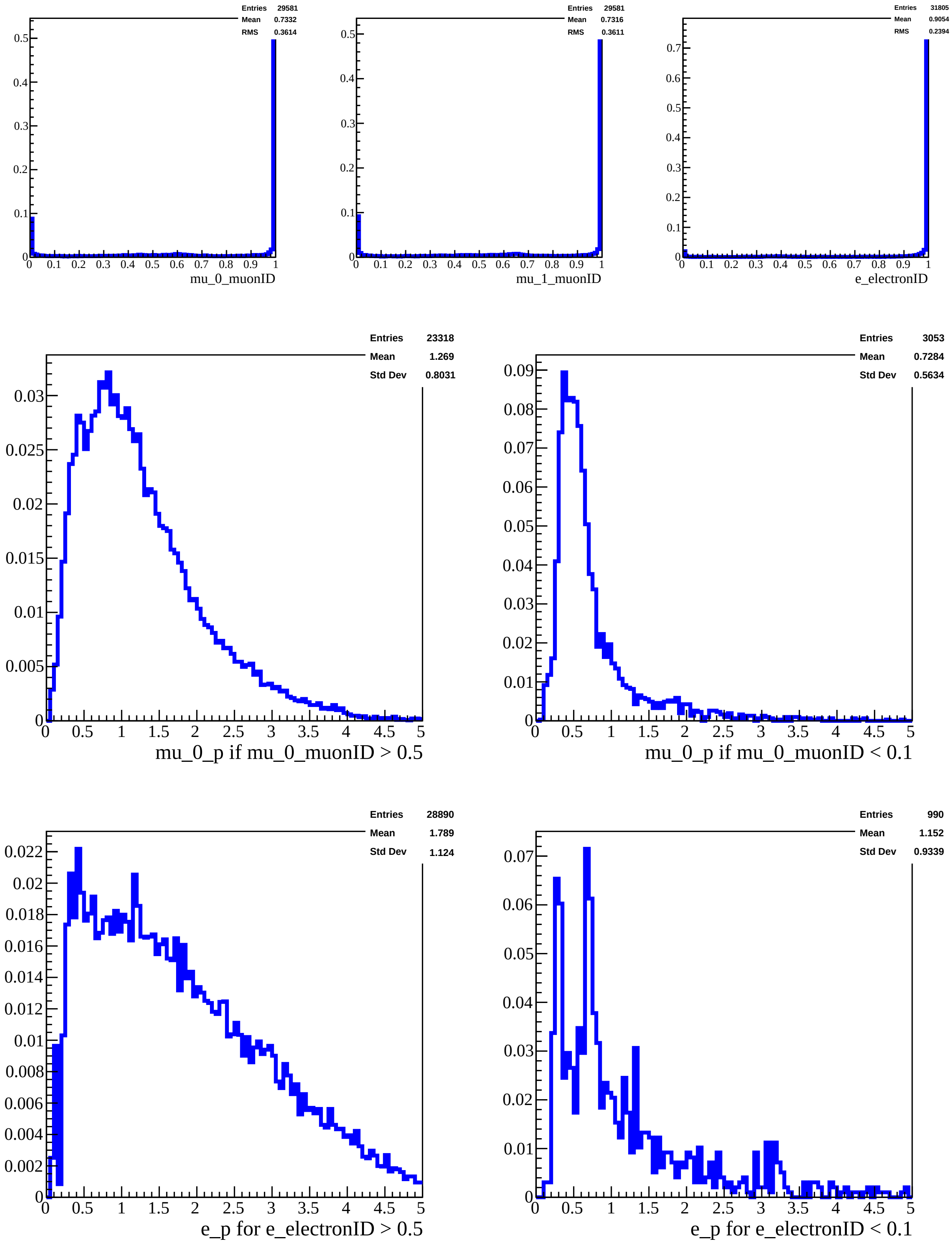

FIG. 33: Belle II lepton ID performances for the signal samples of $m_N = 1000$ MeV

TABLE XIII: The branching fraction $Br(\tau^- \to N\pi^-)$ as a function of the HNL mass for $|V_{\tau N}|^2 = 1$

HNL mass (GeV)	$br(\tau^- \to N\pi^-)$
0.2	250.10716611
0.25	0.10592627
0.275	0.104567
0.3	0.10309155
0.325	0.10150349
0.35	0.099806623
0.375	0.098005062
0.4	0.096103157
0.425	0.094105516
0.45	0.092016986
0.475	0.089842646
0.5	0.087587795
0.525	0.085257939
0.55	0.08285878
0.575	0.080396201
0.6	0.077876256
0.625	0.075305152
0.65	0.072689236
0.675	0.070034978
0.7	0.067348957
0.725	0.064637841
0.75	0.061908372
0.775	0.05916735
0.8	0.056421606
0.825	0.053677993
0.85	0.050943358
0.875	0.048224525
0.9	0.045528274
0.925	0.042861318
0.95	0.040230279
0.975	0.037641667
1.	0.035101856
1.025	0.03261706
1.05	0.030193305
1.075	0.027836405
1.1	0.025551938
1.125	0.023345215
1.15	0.021221255
1.175	0.019184758
1.2	0.01724007
1.225	0.015391161
1.25	0.013641592
1.275	0.011994482
1.3	0.010452482
1.325	0.0090177381
1.35	0.0076918632
1.375	0.0064759024
1.4	0.0053703008
1.425	0.0043748704
1.45	0.0034887568
1.475	0.0027104063
1.5	0.0020375327
1.525	0.0014670828
1.55	0.00099519505
1.575	0.00061711744
1.6	0.00032688486

TABLE XIV: The branching fraction $Br(N \to \mu^+\mu^-\nu_\tau)$ as a function of the HNL mass for $|V_{\tau N}|^2 = 1$

HNL mass (GeV)	$Br(\tau^- \to \mu^+\mu^-\nu_\tau)$
0.225	0.0000037764628
0.25	0.000094673938
0.275	0.00038099178
0.3	0.00089464024
0.325	0.001638705
0.35	0.002587494
0.375	0.003713401
0.4	0.0049975021
0.425	0.0064250842
0.45	0.0079446983
0.475	0.009559162
0.5	0.011272705
0.525	0.012991204
0.55	0.014794949
0.575	0.016582111
0.6	0.01837722
0.625	0.020055846
0.65	0.021790102
0.675	0.023393541
0.7	0.025041682
0.725	0.026631279
0.75	0.028147725
0.775	0.029697193
0.8	0.030922257
0.825	0.031866706
0.85	0.032785284
0.875	0.033681067
0.9	0.03445172
0.925	0.035115506
0.95	0.03575332
0.975	0.036367441
1.	0.03525189
1.025	0.03291937
1.05	0.033283246
1.075	0.033628892
1.1	0.033957696
1.125	0.034270923
1.15	0.034564315
1.175	0.034835458
1.2	0.035093944
1.225	0.035340668
1.25	0.03557645
1.275	0.035802041
1.3	0.036014904
1.325	0.036211503
1.35	0.036399689
1.375	0.036580009
1.4	0.036752964
1.425	0.036919017
1.45	0.037078599
1.475	0.037235705
1.5	0.037396646
1.525	0.037552345
1.55	0.037703114
1.575	0.037849242
1.6	0.037990999

TABLE XV: The product $c\tau$ of the speed of light and the HNL lifetime as a function of the HNL mass for $|V_{\tau N}|^2 = 1$

HNL mass (GeV)	$c\tau$
0.2	3168.9416
0.225	1635.1219
0.25	968.10727
0.275627.83044 0.3	432.12832
0.325	312.45594
0.35	232.93065
0.375	177.89561
0.4	138.81736
0.425	110.38016
0.45	88.771277
0.475	72.333378
0.5	59.712532
0.525	49.526423
0.55	41.55885
0.575	35.021382
0.6	29.699644
0.625	25.187928
0.65	21.558764
0.675	18.457172
0.7	15.928967
0.725	13.793066
0.75	11.977082
0.775	10.466808
0.8	9.0952638
0.825	7.87625
0.85	6.852706
0.875	5.9886415
0.9	5.2394944
0.925	4.5912124
0.95	4.0379663
0.975	3.5637968
1.	3.009908
1.025	2.4586761
1.05	2.1825495
1.075	1.9429384
1.1	1.734321
1.125	1.5521106
1.15	1.392263
1.175	1.2515194
1.2	1.1275544
1.225	1.0180768
1.25	0.92114613
1.275	0.83511389
1.3	0.75850663
1.325	0.69006244
1.35	0.62891329
1.375	0.5741669
1.4	0.52505366
1.425	0.48090796
1.45	0.44115266
1.475	0.40532523
1.5	0.37303789
1.525	0.3438001
1.55	0.31728033
1.575	0.29318769
1.6	0.27126637

[1] Sacha Davidson, Enrico Nardi, and Yosef Nir. Leptogenesis. *Phys. Rept.*, 466:105–177, 2008. doi:10.1016/j.physrep.2008.06.002.

[2] Apostolos Pilaftsis. The little review on leptogenesis. *J. Phys. Conf. Ser.*, 171:012017, 2009. doi:10.1088/1742-6596/171/1/012017.

[3] Mikhail Shaposhnikov. Baryogenesis. *J. Phys. Conf. Ser.*, 171:012005, 2009. doi:10.1088/1742-6596/171/1/012005.

[4] Takehiko Asaka, Steve Blanchet, and Mikhail Shaposhnikov. The νMSM, dark matter and neutrino masses. *Phys. Lett. B*, 631:151–156, 2005. doi:10.1016/j.physletb.2005.09.070.

[5] Takehiko Asaka and Mikhail Shaposhnikov. The νMSM, dark matter and baryon asymmetry of the universe. *Phys. Lett. B*, 620:17–26, 2005. doi:10.1016/j.physletb.2005.06.020.

[6] Alexey Boyarsky, Oleg Ruchayskiy, and Mikhail Shaposhnikov. The Role of sterile neutrinos in cosmology and astrophysics. *Ann. Rev. Nucl. Part. Sci.*, 59:191–214, 2009. doi:10.1146/annurev.nucl.010909.083654.

[7] A. Boyarsky, M. Drewes, T. Lasserre, S. Mertens, and O. Ruchayskiy. Sterile neutrino Dark Matter. *Prog. Part. Nucl. Phys.*, 104:1–45, 2019. doi:10.1016/j.ppnp.2018.07.004.

[8] J. Ghiglieri and M. Laine. Sterile neutrino dark matter via coinciding resonances. *JCAP*, 07:012, 2020. doi:10.1088/1475-7516/2020/07/012.

[9] Armen Tumasyan et al. Search for a right-handed W boson and a heavy neutrino in proton-proton collisions at $\sqrt{s} = 13$ TeV. 12 2021.

[10] Georges Aad et al. Search for heavy neutral leptons in decays of W bosons produced in 13 TeV pp collisions using prompt and displaced signatures with the ATLAS detector. *JHEP*, 10:265, 2019. doi:10.1007/JHEP10(2019)265.

[11] Belle Collaboration. Search for heavy neutrinos at Belle. *Phys. Rev. D*, 87(7):071102, 2013. doi:10.1103/PhysRevD.87.071102. [Erratum: Phys. Rev. D **95**, 099903 (2017)].

[12] NuTeV Collaboration. Search for neutral heavy leptons in a high-energy neutrino beam. *Phys. Rev. Lett.*, 83:4943–4946, 1999. doi:10.1103/PhysRevLett.83.4943.

[13] DELPHI Collaboration. Search for neutral heavy leptons produced in Z decays. *Z. Phys. C*, 74:57–71, 1997. doi:10.1007/s002880050370. [Erratum: Z. Phys. C **75**, 580 (1997)].

[14] CHARM II Collaboration. Search for heavy isosinglet neutrinos. *Phys. Lett. B*, 343:453–458, 1995. doi:10.1016/0370-2693(94)01422-9.

[15] NA3 Collaboration. Mass and lifetime limits on new long-lived particles in 300 GeV/$c\,\pi^-$ interactions. *Z. Phys. C*, 31:21, 1986. doi:10.1007/BF01559588.

[16] CHARM Collaboration. A search for decays of heavy neutrinos in the mass range 0.5-2.8 GeV. *Phys. Lett. B*, 166:473–478, 1986. doi:10.1016/0370-2693(86)91601-1.

[17] WA66 Collaboration. Search for heavy neutrino decays in the BEBC beam dump experiment. *Phys. Lett. B*, 160:207–211, 1985. doi:10.1016/0370-2693(85)91493-5.

[18] CMS Collaboration. Search for long-lived heavy neutral leptons with displaced vertices in proton-proton collisions at $\sqrt{s}$ =13 TeV. 1 2022.

[19] Search for heavy neutral leptons in decays of W bosons using a dilepton displaced vertex in $\sqrt{s} = 13$ TeV pp collisions with the ATLAS detector. 4 2022.

[20] BABAR Collaboration. Search for heavy neutral leptons using tau lepton decays at babar, 2022. URL `https://arxiv.org/abs/2207.09575`.

[21] Mark Thomson. *Modern particle physics*. Cambridge University Press, New York, 2013. ISBN 978-1-107-03426-6.

[22] P. A. Zyla et al. Review of Particle Physics. *PTEP*, 2022(8):083C01, 2022. doi:10.1093/ptep/ptaa104.

[23] Boris Kayser. Neutrino physics. 2005. doi:10.48550/ARXIV.HEP-PH/0506165. URL `https://arxiv.org/abs/hep-ph/0506165`.

[24] Q. R. Ahmad, R. C. Allen, T. C. Andersen, J. D.Anglin, J. C. Barton, E. W. Beier, M. Bercovitch, J. Bigu, S. D. Biller, R. A. Black, I. Blevis, R. J. Boardman, J. Boger, E. Bonvin, M. G. Boulay, M. G. Bowler, T. J. Bowles, S. J. Brice, M. C. Browne, T. V. Bullard, G. Bühler, J. Cameron, Y. D. Chan, H. H. Chen, M. Chen, X. Chen, B. T. Cleveland, E. T. H. Clifford, J. H. M. Cowan, D. F. Cowen, G. A. Cox, X. Dai, F. Dalnoki-Veress, W. F. Davidson, P. J. Doe, G. Doucas, M. R. Dragowsky, C. A. Duba, F. A. Duncan, M. Dunford, J. A.

Dunmore, E. D. Earle, S. R. Elliott, H. C. Evans, G. T. Ewan, J. Farine, H. Fergani, A. P. Ferraris, R. J. Ford, J. A. Formaggio, M. M. Fowler, K. Frame, E. D. Frank, W. Frati, N. Gagnon, J. V. Germani, S. Gil, K. Graham, D. R. Grant, R. L. Hahn, A. L. Hallin, E. D. Hallman, A. S. Hamer, A. A. Hamian, W. B. Handler, R. U. Haq, C. K. Hargrove, P. J. Harvey, R. Hazama, K. M. Heeger, W. J. Heintzelman, J. Heise, R. L. Helmer, J. D. Hepburn, H. Heron, J. Hewett, A. Hime, M. Howe, J. G. Hykawy, M. C. P. Isaac, P. Jagam, N. A. Jelley, C. Jillings, G. Jonkmans, K. Kazkaz, P. T. Keener, J. R. Klein, A. B. Knox, R. J. Komar, R. Kouzes, T. Kutter, C. C. M. Kyba, J. Law, I. T. Lawson, M. Lay, H. W. Lee, K. T. Lesko, J. R. Leslie, I. Levine, W. Locke, S. Luoma, J. Lyon, S. Majerus, H. B. Mak, J. Maneira, J. Manor, A. D. Marino, N. McCauley, A. B. McDonald, D. S. McDonald, K. McFarlane, G. McGregor, R. Meijer Drees, C. Mifflin, G. G. Miller, G. Milton, B. A. Moffat, M. Moorhead, C. W. Nally, M. S. Neubauer, F. M. Newcomer, H. S. Ng, A. J. Noble, E. B. Norman, V. M. Novikov, M. O'Neill, C. E. Okada, R. W. Ollerhead, M. Omori, J. L. Orrell, S. M. Oser, A. W. P. Poon, T. J. Radcliffe, A. Roberge, B. C. Robertson, R. G. H. Robertson, S. S. E. Rosendahl, J. K. Rowley, V. L. Rusu, E. Saettler, K. K. Schaffer, M. H. Schwendener, A. Schülke, H. Seifert, M. Shatkay, J. J. Simpson, C. J. Sims, D. Sinclair, P. Skensved, A. R. Smith, M. W. E. Smith, T. Spreitzer, N. Starinsky, T. D. Steiger, R. G. Stokstad, L. C. Stonehill, R. S. Storey, B. Sur, R. Tafirout, N. Tagg, N. W. Tanner, R. K. Taplin, M. Thorman, P. M. Thornewell, P. T. Trent, Y. I. Tserkovnyak, R. Van Berg, R. G. Van de Water, C. J. Virtue, C. E. Waltham, J.-X. Wang, D. L. Wark, N. West, J. B. Wilhelmy, J. F. Wilkerson, J. R. Wilson, P. Wittich, J. M. Wouters, and M. Yeh. Direct evidence for neutrino flavor transformation from neutral-current interactions in the sudbury neutrino observatory. *Phys. Rev. Lett.*, 89:011301, Jun 2002. doi:10.1103/PhysRevLett.89.011301. URL `https://link.aps.org/doi/10.1103/PhysRevLett.89.011301`.

[25] Y. Fukuda, T. Hayakawa, E. Ichihara, K. Inoue, K. Ishihara, H. Ishino, Y. Itow, T. Kajita, J. Kameda, S. Kasuga, K. Kobayashi, Y. Kobayashi, Y. Koshio, M. Miura, M. Nakahata, S. Nakayama, A. Okada, K. Okumura, N. Sakurai, M. Shiozawa, Y. Suzuki, Y. Takeuchi, Y. Totsuka, S. Yamada, M. Earl, A. Habig, E. Kearns, M. D. Messier, K. Scholberg, J. L. Stone, L. R. Sulak, C. W. Walter, M. Goldhaber, T. Barszczxak, D. Casper, W. Gajewski, P. G. Halverson, J. Hsu, W. R. Kropp, L. R. Price, F. Reines, M. Smy, H. W. Sobel, M. R. Vagins, K. S. Ganezer, W. E. Keig, R. W. Ellsworth, S. Tasaka, J. W. Flanagan, A. Kibayashi, J. G. Learned, S. Matsuno, V. J. Stenger, D. Takemori, T. Ishii, J. Kanzaki, T. Kobayashi, S. Mine, K. Nakamura, K. Nishikawa, Y. Oyama, A. Sakai, M. Sakuda, O. Sasaki, S. Echigo, M. Kohama, A. T. Suzuki, T. J. Haines, E. Blaufuss, B. K. Kim, R. Sanford, R. Svoboda, M. L. Chen, Z. Conner, J. A. Goodman, G. W. Sullivan, J. Hill, C. K. Jung, K. Martens, C. Mauger, C. McGrew, E. Sharkey, B. Viren, C. Yanagisawa, W. Doki, K. Miyano, H. Okazawa, C. Saji, M. Takahata, Y. Nagashima, M. Takita, T. Yamaguchi, M. Yoshida, S. B. Kim, M. Etoh, K. Fujita, A. Hasegawa, T. Hasegawa, S. Hatakeyama, T. Iwamoto, M. Koga, T. Maruyama, H. Ogawa, J. Shirai, A. Suzuki, F. Tsushima, M. Koshiba, M. Nemoto, K. Nishijima, T. Futagami, Y. Hayato, Y. Kanaya, K. Kaneyuki, Y. Watanabe, D. Kielczewska, R. A. Doyle, J. S. George, A. L. Stachyra, L. L. Wai, R. J. Wilkes, and K. K. Young. Evidence for oscillation of atmospheric neutrinos. *Phys. Rev. Lett.*, 81:1562–1567, Aug 1998. doi:10.1103/PhysRevLett.81.1562. URL `https://link.aps.org/doi/10.1103/PhysRevLett.81.1562`.

[26] Peter Minkowski. $\mu \to e\gamma$ at a rate of one out of 10^9 muon decays,. *Phys. Lett. B*, 67:421–428, 1977. doi:10.1016/0370-2693(77)90435-X.

[27] Tsutomu Yanagida. Horizontal gauge symmetry and masses of neutrinos. *Conf. Proc. C*, 7902131:95–99, 1979.

[28] S. L. Glashow. The Future of Elementary Particle Physics. *NATO Sci. Ser. B*, 61:687, 1980. doi:10.1007/978-1-4684-7197-7˙15.

[29] Murray Gell-Mann, Pierre Ramond, and Richard Slansky. Complex Spinors and Unified Theories. *Conf. Proc. C*, 790927:315–321, 1979.

[30] Rabindra N. Mohapatra and Goran Senjanovic. Neutrino Mass and Spontaneous Parity Nonconservation. *Phys. Rev. Lett.*, 44:912, 1980. doi:10.1103/PhysRevLett.44.912.

[31] J. Schechter and J. W. F. Valle. Neutrino Masses in SU(2) x U(1) Theories. *Phys. Rev. D*, 22:2227, 1980. doi:10.1103/PhysRevD.22.2227.

[32] J. Schechter and J. W. F. Valle. Neutrino Decay and Spontaneous Violation of Lepton Number. *Phys. Rev. D*, 25:774, 1982. doi:10.1103/PhysRevD.25.774.

[33] C. O. Dib, J. C. Helo, M. Nayak, N. A. Neill, A. Soffer, and J. Zamora-Saa. Searching for a sterile neutrino that mixes predominantly with ν_τ at B factories. *Phys. Rev. D*, 101(9): 093003, 2020. doi:10.1103/PhysRevD.101.093003.

[34] Claudio O. Dib, C.S. Kim, Nicolás A. Neill, and Xing-Bo Yuan. the LHC. *Physical Review D*, 97(3), feb 2018. doi:10.1103/physrevd.97.035022. URL `https://doi.org/10.1103%2Fphysrevd.97.035022`.

[35] Michael Gronau, C. N. Leung, and Jonathan L. Rosner. Extending limits on neutral heavy leptons. *Phys. Rev. D*, 29:2539–2558, Jun 1984. doi:10.1103/PhysRevD.29.2539. URL `https://link.aps.org/doi/10.1103/PhysRevD.29.2539`.

[36] S. Kurokawa and E. Kikutani. Overview of the kekb accelerators. *Nuclear Instruments and Methods in Physics Research Section A: Accelerators, Spectrometers, Detectors and Associated Equipment*, 499(1):1–7, 2003. ISSN 0168-9002. doi:https://doi.org/10.1016/S0168-9002(02)01771-0. URL `https://www.sciencedirect.com/science/article/pii/S0168900202017710`. KEK-B: The KEK B-factory.

[37] Jolanta Brodzicka, Thomas Browder, Paoti Chang, Simon Eidelman, Bostjan Golob, Kiyoshi Hayasaka, Hisaki Hayashii, Toru Iijima, Kenji Inami, Kay Kinoshita, Youngjoon Kwon, Kenkichi Miyabayashi, Gagan Mohanty, Mikihiko Nakao, Hideyuki Nakazawa, Stephen Olsen, Yoshihide Sakai, Christoph Schwanda, Alan Schwartz, Karim Trabelsi, Sadaharu Uehara, Shoji Uno, Yasushi Watanabe, Anze Zupanc, and for the Belle Collaboration. Physics achievements from the Belle experiment. *Progress of Theoretical and Experimental Physics*, 2012(1), 12 2012. ISSN 2050-3911. doi:10.1093/ptep/pts072. URL `https://doi.org/10.1093/ptep/pts072`. 04D001.

[38] Swagato Banerjee, Bolek Pietrzyk, J. Michael Roney, and Zbigniew Was. Tau and muon pair production cross-sections in electron-positron annihilations at s**(1/2) = 10.58-GeV. *Phys. Rev. D*, 77:054012, 2008. doi:10.1103/PhysRevD.77.054012.

[39] A. Abashian, K. Gotow, N. Morgan, L. Piilonen, S. Schrenk, K. Abe, I. Adachi, J.P. Alexander, K. Aoki, S. Behari, Y. Doi, R. Enomoto, H. Fujii, Y. Fujita, Y. Funahashi, J. Haba, H. Hamasaki, T. Haruyama, K. Hayashi, Y. Higashi, N. Hitomi, S. Igarashi, Y. Igarashi, T. Iijima, Hirokazu Ikeda, Hitomi Ikeda, R. Itoh, M. Iwai, H. Iwasaki, Y. Iwasaki, K.K. Joo, K. Kasami, N. Katayama, M. Kawai, H. Kichimi, T. Kobayashi, S. Koike, Y. Kondo, M.H. Lee, Y. Makida, A. Manabe, T. Matsuda, T. Murakami, S. Nagayama, M. Nakao, T. Nozaki, K. Ogawa, R. Ohkubo, Y. Ohnishi, H. Ozaki, H. Sagawa, M. Saito, Y. Sakai, T. Sasaki, N. Sato, T. Sumiyoshi, J. Suzuki, J.I. Suzuki, S. Suzuki, F. Takasaki, K. Tamai, M. Tanaka, T. Tatomi, T. Tsuboyama, K. Tsukada, T. Tsukamoto, S. Uehara, N. Ujiie, S. Uno, B. Yabsley,

Y. Yamada, H. Yamaguchi, H. Yamaoka, Y. Yamaoka, M. Yamauchi, Y. Yoshimura, H. Zhao, R. Abe, G. Iwai, T. Kawasaki, H. Miyata, K. Shimada, S. Takahashi, N. Tamura, K. Abe, H. Hanada, T. Nagamine, M. Nakajima, T. Nakajima, S. Narita, M. Sanpei, T. Takayama, M. Ueki, M. Yamaga, A. Yamaguchi, B.S. Ahn, J.S. Kang, Hyunwoo Kim, C.W. Park, H. Park, H.S. Ahn, H.K. Jang, C.H. Kim, S.K. Kim, S.H. Lee, C.S. Park, E. Won, H. Aihara, T. Higuchi, H. Kawai, T. Matsubara, T. Nakadaira, H. Tajima, J. Tanaka, T. Tomura, M. Yokoyama, M. Akatsu, K. Fujimoto, M. Hirose, K. Inami, A. Ishikawa, S. Itami, T. Kani, T. Matsumoto, I. Nagai, T. Okabe, T. Oshima, K. Senyo, A. Sugi, A. Sugiyama, S. Suitoh, S. Suzuki, M. Tomoto, K. Yoshida, R. Akhmetshin, P. Chang, Y. Chao, Y.Q. Chen, W.S. Hou, S.C. Hsu, H.C. Huang, T.J. Huang, M.C. Lee, R.S. Lu, J.C. Peng, K.C. Peng, S. Sahu, H.F. Sung, K.L. Tsai, K. Ueno, C.C. Wang, M.Z. Wang, G. Alimonti, T.E. Browder, B.C.K. Casey, F. Fang, H. Guler, M. Jones, Y. Li, S.L. Olsen, M. Peters, J.L. Rodriguez, M. Rosen, S. Swain, K. Trabelsi, G. Varner, H. Yamamoto, Y.H. Zheng, Q. An, H.F. Chen, Y.F. Wang, Z.Z. Xu, S.W. Ye, Z.P. Zhang, M. Asai, Y. Asano, S. Mori, S. Stanič, Y. Tsujita, J. Zhang, D. Žontar, T. Aso, V. Aulchenko, D. Beiline, A. Bondar, L. Dneprovsky, S. Eidelman, A. Garmash, A. Kuzmin, L. Romanov, N. Root, B. Shwartz, A. Sidorov, V. Sidorov, Y. Usov, V. Zhilich, A.M. Bakich, L.S. Peak, K.E. Varvell, E. Banas, A. Bozek, P. Jalocha, P. Kapusta, Z. Natkaniec, W. Ostrowicz, H. Palka, M. Rozanka, K. Rybicki, P.K. Behera, A. Mohapatra, M. Satapathy, Y.H. Chang, H.S. Chen, L.Y. Dong, J. Li, H.M. Liu, Z.P. Mao, C.X. Yu, C.C. Zhang, S.Q. Zhang, Z.G. Zhao, Z.P. Zheng, B.G. Cheon, Y. Choi, D.W. Kim, J.W. Nam, S. Chidzik, K. Korotuschenko, C. Leonidopoulos, T. Liu, D. Marlow, C. Mindas, E. Prebys, R. Rabberman, W. Sands, R. Wixted, S. Choi, J. Dragic, C.W. Everton, A. Gordon, N.C. Hastings, E.M. Heenan, L.C. Moffitt, G.R. Moloney, G.F. Moorhead, M.E. Sevior, G.N. Taylor, S.N. Tovey, A. Drutskoy, R. Kagan, P. Pakhlov, S. Semenov, C. Fukunaga, R. Suda, M. Fukushima, V.I. Goriletsky, B.V. Grinyov, V.R. Lyubinsky, A.I. Panova, K.V. Shakhova, L.I. Shpilinskaya, E.L. Vinograd, B.G. Zaslavsky, R.S. Guo, F. Haitani, Y. Hoshi, K. Neichi, K. Hara, T. Hara, M. Hazumi, T. Hojo, D. Jackson, H. Miyake, Y. Nagashima, J. Ryuko, K. Sumisawa, M. Takita, T. Yamanaka, H. Hayashii, K. Miyabayashi, S. Noguchi, S. Hikita, H. Hirano, K. Hoshina, H. Mamada, O. Nitoh, N. Okazaki, T. Yokoyama, H. Ishino, S. Ichizawa, T. Hirai, H. Kakuno, J. Kaneko, T. Nakamura, Y. Ohshima, Y. Watanabe, S. Yanaka, Y. Inoue, E. Nakano, T. Takahashi, Y. Teramoto, J.H. Kang, H.J. Kim, Heejong Kim, Y.-J. Kwon, H. Kawai, E. Kurihara, T. Ooba, K. Suzuki, Y. Unno, N. Kawamura, H. Yuta, K. Kinoshita, A. Satpathy, S. Kobayashi, T. Kuniya, A. Murakami, T. Tsukamoto, S. Kumar, J. Singh, J. Lange, R. Stock, S. Matsumoto, M. Watanabe, H. Matsuo, S. Nishida, T. Nomura, H. Sakamoto, N. Sasao, Y. Ushiroda, Y. Nagasaka, Y. Tanaka, S. Ogawa, H. Shibuya, K. Hanagaki, S. Okuno, D.Z. Shen, D.S. Yan, Z.W. Yin, N. Tan, C.H. Wang, T. Yamaki, and Y. Yamashita. The belle detector. *Nuclear Instruments and Methods in Physics Research Section A: Accelerators, Spectrometers, Detectors and Associated Equipment*, 479(1): 117–232, 2002. ISSN 0168-9002. doi:https://doi.org/10.1016/S0168-9002(01)02013-7. URL `https://www.sciencedirect.com/science/article/pii/S0168900201020137`. Detectors for Asymmetric B-factories.

[40] E Nakano. Belle pid. *Nuclear Instruments and Methods in Physics Research Section A: Accelerators, Spectrometers, Detectors and Associated Equipment*, 494(1):402–408, 2002. ISSN 0168-9002. doi:https://doi.org/10.1016/S0168-9002(02)01510-3. URL `https://www.sciencedirect.com/science/article/pii/S0168900202015103`. Proceedings of the 8th International Conference on Instrumentatio n for Colliding Beam Physics.

[41] Belle 2 software documentation. https://software.belle2.org/sphinx/release-06-00-02/index.html. Accessed: 2022-04-08.

[42] Keck T. Prim M. et al. Gelb, M. B2BII: Data Conversion from Belle to Belle II. *Comput Softw Big Sci*, 2(9), 2018. doi:10.1007/s41781-018-0016-x. URL https://doi.org/10.1007/s41781-018-0016-x.

[43] Lukas Heinrich, Matthew Feickert, and Giordon Stark. pyhf: v0.7.0. URL https://doi.org/10.5281/zenodo.1169739. https://github.com/scikit-hep/pyhf/releases/tag/v0.7.0.

[44] Lukas Heinrich, Matthew Feickert, Giordon Stark, and Kyle Cranmer. pyhf: pure-python implementation of histfactory statistical models. *Journal of Open Source Software*, 6(58): 2823, 2021. doi:10.21105/joss.02823. URL https://doi.org/10.21105/joss.02823.

[45] Kyle Cranmer, George Lewis, Lorenzo Moneta, Akira Shibata, and Wouter Verkerke. HistFactory: A tool for creating statistical models for use with RooFit and RooStats. Technical report, New York U., New York, Jan 2012. URL https://cds.cern.ch/record/1456844.

[46] Kyrylo Bondarenko, Alexey Boyarsky, Dmitry Gorbunov, and Oleg Ruchayskiy. Phenomenology of GeV-scale Heavy Neutral Leptons. *JHEP*, 11:032, 2018. doi:10.1007/JHEP11(2018)032.

[47] Belle website. https://belle.kek.jp/group/ecl/private/lum/lum6new.html.

[48] S. Jadach, B.F.L. Ward, and Z. Wacs. The precision monte carlo event generator for two-fermion final states in collisions. *Computer Physics Communications*, 130(3):260–325, aug 2000. doi:10.1016/s0010-4655(00)00048-5. URL https://doi.org/10.1016%2Fs0010-4655%2800%2900048-5.

[49] Torbjörn Sjöstrand, Patrik Edén, Christer Friberg, Leif Lönnblad, Gabriela Miu, Stephen Mrenna, and Emanuel Norrbin. High-energy-physics event generation with pythia 6.1. *Computer Physics Communications*, 135(2):238–259, apr 2001. doi:10.1016/s0010-4655(00)00236-8. URL https://doi.org/10.1016%2Fs0010-4655%2800%2900236-8.

[50] Tenchini, Francesco and Krohn, Jo-Frederik. Decay chain reconstruction at belle ii. *EPJ Web Conf.*, 214:06023, 2019. doi:10.1051/epjconf/201921406023. URL https://doi.org/10.1051/epjconf/201921406023.

[51] Wouter D. Hulsbergen. Decay chain fitting with a kalman filter. *Nuclear Instruments and Methods in Physics Research Section A: Accelerators, Spectrometers, Detectors and Associated Equipment*, 552(3):566–575, nov 2005. doi:10.1016/j.nima.2005.06.078. URL https://doi.org/10.1016%2Fj.nima.2005.06.078.

[52] J.-F. Krohn, F. Tenchini, P. Urquijo, F. Abudinén, S. Cunliffe, T. Ferber, M. Gelb, J. Gemmler, P. Goldenzweig, T. Keck, I. Komarov, T. Kuhr, L. Ligioi, M. Lubej, F. Meier, F. Metzner, C. Pulvermacher, M. Ritter, U. Tamponi, and A. Zupanc. Global decay chain vertex fitting at belle II. *Nuclear Instruments and Methods in Physics Research Section A: Accelerators, Spectrometers, Detectors and Associated Equipment*, 976:164269, oct 2020. doi:10.1016/j.nima.2020.164269. URL https://doi.org/10.1016%2Fj.nima.2020.164269.

[53] R. E. Kalman. A New Approach to Linear Filtering and Prediction Problems. *Journal of Basic Engineering*, 82(1):35–45, 03 1960. ISSN 0021-9223. doi:10.1115/1.3662552.

[54] M. Boglione, J. O. Gonzalez-Hernandez, and A. Simonelli. Transverse momentum dependent fragmentation functions from recent belle data. *Phys. Rev. D*, 106:074024, Oct 2022. doi:10.1103/PhysRevD.106.074024. URL https://link.aps.org/doi/10.1103/PhysRevD.106.074024.

[55] J. Alwall, R. Frederix, S. Frixione, V. Hirschi, F. Maltoni, O. Mattelaer, H.-S. Shao, T. Stelzer, P. Torrielli, and M. Zaro. The automated computation of tree-level and next-to-leading order differential cross sections, and their matching to parton shower simulations. *Journal of High*

Energy Physics, 2014(7), jul 2014. doi:10.1007/jhep07(2014)079. URL https://doi.org/10.1007%2Fjhep07%282014%29079.

[56] R Ruiz; Alva, O. Mattelear T. Han; C. Degrande, J. Turner; S. Pascoli, C. Weiland;, and J. de Vries K. Fuyuto E. Mereghetti V. Cirigliano, W. Dekens. The standard model + heavy neutrinos at NLO in QCD. https://feynrules.irmp.ucl.ac.be/wiki/HeavyN.

[57] D. Sahoo et al. Search for lepton-number- and baryon-number-violating tau decays at Belle. *Phys. Rev. D*, 102:111101, 2020. doi:10.1103/PhysRevD.102.111101.

[58] Y. Jin et al. Observation of $\tau^- \to \pi^- \nu_\tau e^+ e^-$ and search for $\tau^- \to \pi^- \nu_\tau \mu^+ \mu^-$. *Phys. Rev. D*, 100(7):071101, 2019. doi:10.1103/PhysRevD.100.071101.

תקציר

קיימת מוטיבציה גבוהה למציאת לפטונים ניטרלים כבדים (Heavy Neutral Leptons - HNLs), שיכולים להיות הפתרון לבעיות המסה של הניטרונים, החומר האפל והאסימטריה הבריונית ביקום. ניסויים קודמים הצליחו לקבוע גבולות צפופים על ערבוב (mixing) של HNL עם חלקיקי ניטרינו אלקטרוני ומואוני. היות שכך, אנו מחפשים את HNL המתערבב בעיקר עם חלקיקי ניטרינו טאואוני. HNL שכזה יכול להיות מיוצר בדעיכות של חלקיקי טאו, והמקום הטוב ביותר לחקור אותם הוא במפעלי B (B-factories). החיפוש שלנו מתבצע בדגימות של 10^8 אירועים של $e^+e^- \to \tau^+\tau^-$ עם אנרגיית מרכז מסה של 10.58 GeV, אשר נאספו ע״י בל (Belle). החיפוש מתמקד בחלקיקי HNL בעלי זמן חיים ארוך, ובטווח מסה של 0.3-1.6 GeV, כך שאנו מנצלים חתימה של קודקוד מרוחק (Displaced Vertex) כדי לצמצם את הרקע. אנו מציבים צפי לגבול חדש על הערבוב בין HNL לניטרינו טאואוני.

הפקולטה למדעים
מדויקים ע"ש ריימונד
ובברלי סאקלר
אוניברסיטת תל אביב

בית הספר לפיזקה ואסטרונומיה

חיפוש אחר לפטון ניטרלי כבד שמתערבב בעיקר עם ניטרוני טאואוני

חיבור זה הוגש כחלק מהדרישות לקבלת התואר
"מוסמך אוניברסיטה" – M.Sc.

על ידי

אורי ישראל פוגל

העבודה נכתבה בהדרכתו של

פרופ' אבנר סופר